Minimizing Motions of Floating Vessels Using the Moving Frame Method in Dynamics

Håkon Teigland
Andreas Flåten
Martin R. Lied
Caspar C. Smith
Joakim F. Nyland

Bachelor's thesis in Marine Technology
Bergen, Norway 2017

Minimizing Motions of Floating Vessels Using the Moving Frame Method in Dynamics

Håkon Teigland
Andreas Flåten
Martin R. Lied
Caspar C. Smith
Joakim F. Nyland

Department of Mechanical- and Marine Engineering
Western Norway University of Applied Sciences
NO-5063 Bergen, Norway

Høgskulen på Vestlandet
Avdeling for ingeniør- og økonomifag
Institutt for maskin- og marinfag
Inndalsveien 28,
NO-5063 Bergen, Norge

Norsk tittel:	Minimering av bevegelser til flytende fartøy ved bruk av "the Moving Frame Method in Dynamics"
Authors, student number:	Håkon Teigland, h146618 Andreas Flåten, h143270 Martin R. Lied, h144169 Caspar C. Smith, h124266 Joakim F. Nyland, h147044
Study program:	14 HMMT Marine Technology/14 HUVT-F Subsea Technology
Date:	06 2017
Report number:	IMM 2017-M34
Supervisor at HVL:	Thomas J. Impelluso, Johnny J. Jørgensen
Assigned by:	Thomas J. Impelluso, AKVA Group ASA
Contact person:	Andrés Lara
Antall filer levert digitalt:	1

1 Abstract

This Bachelor Thesis presents a new method in dynamics, The Moving Frame Method (MFM), and uses it to investigate the effects of gyroscopic stabilizers on a barge. In collaboration with AKVA Group, a scale model of a barge, used in fish farming, is tested, to determine the hydrodynamic properties of the barge. The same model is then used to validate the theoretical analysis on gyroscopic stabilizers.

Considering the increase in Norway's aquaculture [1], which has led to fish farming sites moving further offshore, there is a need for reducing roll motions of the floating vessels. One way of addressing this challenge is using gyroscopic stabilizers (inertial spinning disks), mounted on the vessels. By use of the MFM, the equations of motions are derived and numerically integrated, using fourth order Runge-Kutta. From the theoretical analysis, it is shown that the gyroscopes induce a rolling moment, which can be used to limit the motions of the barge in waves. The theoretical analyses are modelled and visualized on a 3D web page (Appendix F, http://home.hib.no/prosjekter/dynamics/2017/gyroscope/). Also, two papers are being published, by the authors, at the ASME 2017 International Mechanical Engineering Congress & Exposition. One of these presents the theory [2] and the other one [3] presents the experiment.

A scale model of one of AKVA Group's feed barges are built, to be tested at the wave tank at HVL (Western Norway University of Applied Science). The natural period and response amplitude operators of the model are found. In addition, the model is tested in irregular seas. The tests performed are done for various loading conditions and directions. Some of the test results are compared with simulated data from MOSES, an offshore simulation software.

The lightship natural roll period of the barge is found to be close to the peak period of the 10 and 50 year waves. This leads to large roll motions and it is suggested that measures are taken to alter the natural period of the barge. One such method is to use ballasting tanks, which are found to reduce motions of the model. The simulated data is found to give an indication of how the full-scale barge will behave. However, the simulated data do not give an accurate description of motions experienced by the model.

Further measures to reduce roll can be taken by installing bilge keels, on the barge. The effects of these are simulated in MOSES and compared to simulated data, performed on a barge without bilge keels. The simulated data shows that roll angles, angular roll velocity and angular roll accelerations are reduced by up to 8%, by installing bilge keels.

Finally, a dual gyroscopic stabilization system is installed on the model, to validate the theoretical analysis. The gyroscopes consist of spinning flywheels, that are precessed by servomotors, controlled by microcontrollers. The moment exerted from the gyroscopes, on the model, proved too small to acquire measurable motions of the barge. However, observations made by the authors, confirmed the qualitative results found from the theoretical analysis.

2 Sammendrag

Denne bacheloroppgaven presenterer en ny metode innenfor dynamikk, kalt "The Moving Frame Method" (MFM), og bruker den til å undersøke effektene fra gyroskopiske stabilisatorer på en flåte. I samarbeid med AKVA Group blir en modell av en flåte, brukt i oppdrett, testet for å bestemme de hydrodynamiske egenskapene til flåten. Den samme modellen blir brukt til å sjekke de teoretiske analysene gjort om gyroskopiske stabilisatorer.

Med tanke på økningen i Norges akvakultur [1], som har ført til at fiskeoppdrett flyttes lenger fra kysten, er det et behov for å redusere bevegelser av flytende fartøy. En måte å møte dette behovet på er å bruke gyroskopiske stabilisatorer (roterende metallskiver), montert på fartøyene. Bevegelsesligningene utledes ved å bruke MFM og integreres ved å bruke 4. ordens Runge-Kutta. Fra de teoretiske analysene vises det at gyroskopene skaper et krengende moment, som kan bli brukt til å begrense bevegelsene til flåten, i bølger. De teoretiske analysene modelleres og visualiseres på en 3D webside (Appendix F, http://home.hib.no/prosjekter/dynamics/2017/gyroscope/). I tillegg blir det publisert to artikler under "ASME 2017 International Mechanical Engineering Congress & Exposition". Hvor den ene presenterer teorien [2] og den andre presenterer eksperimentet [3].

En skalert modell av en av AKVA Groups fôringsflåter bygges, for å bli testet i bølgetanken på Høgskolen på Vestlandet (HVL). Egenperioden og respons amplitude operatorene (RAO) til modellen blir funnet. I tillegg, blir modellen testet i irregulær sjø. Testene gjennomføres i ulike lastkondisjoner og med bølger fra ulike retninger. Noen av testresultatene sammenlignes med simulert data fra MOSES, et offshore-simulasjonsprogram.

Egenperioden i rull (lettskip) er funnet til å være nær peakperioden til 10- og 50 års-bølgene. Dette fører til store rullbevegelser og det foreslås at det gjøres tiltak for å endre egenperioden til flåten. Et mulig tiltak er å bruke ballasteringstanker, som viser seg å begrense bevegelsene til modellen. Den simulerte dataen gir en indikasjon på hvordan den faktiske flåten vil oppføre seg, men den simulerte dataen gir ikke et nøyaktig beskrivelse av bevegelsene til flåten.

Videre tiltak for å redusere rull kan bli gjort ved å installere slingrekjøler på flåten. Effekten fra disse er simulert i MOSES og sammenlignet med simulert data, uten slingrekjøler. Simulasjonene viser at krengevinkel, krengehastighet og krengeakselerasjon reduseres med opptil 8% ved å installere slingrekjøler.

Til slutt installeres et gyroskopisk stabiliseringssystem på modellen, for å sjekke de teoretiske analysene. Gyroskopene består av spinnende svinghjul, som vinkles av servomotorer, kontrollert av en mikrokontroll. Momentet fra gyroskopene, på modellen, er for små til å oppnå målbare bevegelser av flåten. Allikevel så bekrefter observasjoner, gjort av forfatterne, de kvalitative resultatene fra de teoretiske analysene.

3 Table of contents

4 Preface

The thesis is written by a group of students at Western Norway University of Applied Sciences, Department of Mechanical and Marine Engineering. The main topics in this thesis concern marine technology and hydrodynamics with Thomas Impelluso and Johnny Jørgensen as internal supervisors, respectively. Tasks are given by AKVA Group and professor Thomas Impelluso and students have combined the two tasks to one thesis. Andrés Lara has been the external supervisor of this project.

At the start of this project, AKVA Group was building a new feed barge and wanted to investigate its hydrodynamic properties. The feed barge is designed for extreme weather and is modelled without practical testing. Thus, AKVA Group wanted the authors to build a scaled model of the feed barge and test the model in various weather and wave conditions.

The other task presented in this thesis is based on minimizing motions of different types of vessels. The Moving Frame Method in Dynamics, developed by H. Murakami and T. Impelluso, is used to inspect how gyroscopes affect motions on floating vessels.

We would like to give our thanks to the following for their contributions to the research. To AKVA Group ASA represented by Andrés Lara and Ignacio Petkovic, for agreeing to take part in this Bachelor project and providing necessary information along the way. Special thanks are given to Andrés Lara for agreeing to be the external supervisor for this project. To Thomas J. Impelluso and Johnny J. Jørgensen, for being the mentors from HVL. Thomas Impelluso has provided expertise on the Moving Frame Method and Johnny Jørgensen has provided help on the hydrodynamic testing and the use of these results. To Gloria Stenfelt and Harald Moen for helping with hydrodynamic experiments in the wave-tank at HVL.

At last we would like to thank Western Norway University of Applied Sciences for three years of education.

5 Nomenclature

GM – Metacentric height.

KG – Vertical distance from keel to center of gravity.

I – Second moment of area.

∇ - Displaced volume.

Δ – Displaced mass.

ρ – Density.

λ – Scaling factor.

LOA – Length over all.

Tp – Peak Period.

Hs – Significant wave height.

$X_{1/3}$ – 1/3rd significant response.

$( )_M$ – Scaled model.

$( )_F$ – Full size model.

DIR1 – Mooring configuration with waves toward starboard.

DIR2 – Mooring configuration with waves toward a 30 degree offset from the bow, toward starboard.

DIR3 – Mooring configuration with waves toward the bow.

LC0 – Light ship loading condition.

LC1 – Light ship, with ballast, loading condition.

LC2 – Full ship loading condition.

J – Mass moment of inertia.

k – Radius of gyration.

HVL – Høgskulen på Vestlandet - Western Norway University of Applied Science.

MFM – Moving Frame Method in Dynamics.

SO(3) – Special Orthogonal Group.

SE(3) – Special Euclidean Group.

6 Introduction

In recent years, Norway's aquaculture has risen and become an important industry [1]. This has led to an increase in fish farming equipment along the coast, which are pushing farming sites further offshore. This creates a demand for more robust equipment. A traditional farming site consists of several fish cages and a feed barge, used for storage and distribution of feed to the cages. Despite the industry having experienced an increase in automated systems and processes, there are still tasks that demands manual labor. This means that workers needs to work and live on the feed

barges, which puts demands on the motions experienced by the barges.

There are several ways of minimizing motions experienced by a barge or ship, especially in roll. One of these methods is by the use of gyroscopic stabilizers. These have been used for over a century, with the first large ship to use these systems being the USS Henderson, launched in 1916. Despite this, developing the equations of motion for a ship with gyroscopic stabilizers can be difficult. However, by using the Moving Frame Method in Dynamics (MFM) [4], developed by H. Murakami and T. Impelluso, the equations of motion can be derived in a systematic way. The MFM uses the special orthogonal group (SO(3)) and the special Euclidean group (SE(3)) to describe the kinematics and kinetics of bodies, interconnected by joints and forces. This paper uses the MFM to develop the equations of motion for a feed barge with two gyroscopic stabilizers. Further, numerical analysis is done to obtain a simulation of the barge. When being presented with the equations of motion, simulations of the barge can easily be presented on a 3D web canvas by using the Web Graphics Library (WebGL). One such simulation are presented on HVL's web server [3].

In order to verify the numerical simulations obtained, this project uses the wave tank at HVL to perform experimental analysis of a scaled barge model with two gyroscopic stabilizers. To be able to get realistic results, the scaled model has been built based on an actual feed barge. One of the companies designing and building these feed barges are AKVA Group. AKVA Group is the world leading supplier and developer of fish farming equipment and is based in Bryne, Norway. In collaboration with AKVA Group this paper studies the hydrodynamic properties of a new feed barge model to be able to compare the barge motions with and without the gyroscopic stabilizers.

Using a wave tank to test ships and equipment is time consuming and costly. An alternative to doing real life experiments, is to use an offshore simulation software. However, it is difficult to know how accurate these software are. Therefore, this paper compares the results obtain from the experimental tests to simulated results from MOSES, an offshore simulation software.

7 Theory

7.1 Model System Description

Fig. 1 presents the model system under consideration, a system consisting of a ship, equipped with dual gyroscopic roll stabilizers.

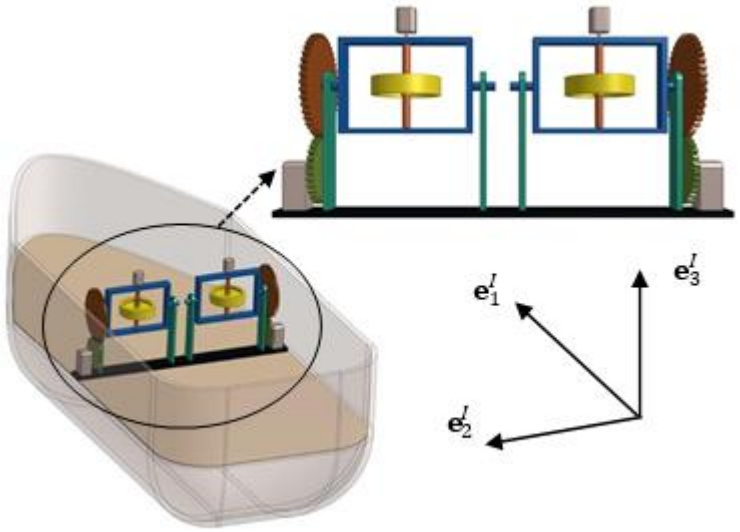

Figure 1: The model system, consisting of an outer body, equipped with dual gyroscopic stabilizers [5].

Each gyroscope consists of a central rotor (the yellow disks, shown in Fig. 1), operated by a motor. For each disk, Fig. 1 shows a gimbal-housing driven by a motor with an attached gear system. Both systems are bolted to the deck or platform of the body. The major components of the system that will be included in the analysis will be the outer body, gimbals, and rotors. The MFM is applied to analyse this problem.

As the gimbal precesses around one axis and the rotor spins around a second axis, a gyroscopic moment is produced around the third axis. The MFM reveals this motion more naturally and will be presented along with the kinetics of joints.

In this study, the MFM employs the Special Euclidean Group, $SE(3)$ and extends previous work by Oscar Rios [5] and [6]. Further details and applications of this can be found in references [7], [8], [9] and [10].

7.2 Moving Frame Method

The MFM replaces an inordinate reliance on vector algebra with the framework of Lie algebra reduced to the simplicity of rotation matrices. It abandons the inertial frame in favour of the moving frame as a formative element. It simplifies variational methods for Hamilton's Principle by

developing a restricted variation of the angular velocity. Finally, it adopts a new compact notation derived from the discipline of geometrical physics that enables the transition from vector algebra to matrix manipulations. The MFM commences with 3D problems and solves them in a direct, matrix-based, straightforward manner that is eminently comprehensible to the average undergraduate.

The system under current analysis will be a linked system: one that progresses from the ship body to the gimbal frame and then the disk itself. Thus, this amounts to a linked system. This kinematic analysis of jointed rigid bodies has been performed using matrices of homogeneous transformations, as presented by Denavit and Hartenberg in 1955 [11]. The matrices of such transformations have been used to define position and velocities of connection points of the system, for example [12], [13], [14], [15] and [16]. However, a more systematic method of computing multibody kinematics is needed; and one with more powerful notation.

The usage of Lie group theory of $SE(3)$ and $se(3)$ in rigid-body dynamics was developed in the physics of relativity and differential geometry [17]. Élie Cartan wrote a basis of vectors and tensors explicitly and referred to frames. Other researchers were using the indicial notation without showing the coordinate basis. Cartan's moving frame method simplified the computation of each connection between a pair of overlapping coordinate systems by an order of magnitude, for example, [10].

Notable applied mathematicians demonstrated the usage of Lie group theories involving the special orthogonal group, $SO(3)$, and the special Euclidean group $SE(3)$ for a single rigid body, for example [18], [19], [20] and [21]. Robotics engineers also employed SE (3) to describe kinematics using without writing coordinate bases explicitly, for example [22], [23] and [24]. Their Lie group computations involve complex adjoint operations. By writing coordinate vector bases explicitly, one can minimize the complexity of the Lie group computations.

An inertial Cartesian coordinate system $\{x_1 \quad x_2 \quad x_3\}$, along with the inertial vector basis $\boldsymbol{e}^I = (\boldsymbol{e}_1^I \quad \boldsymbol{e}_2^I \quad \boldsymbol{e}_3^I)$, are defined, as shown in Fig. 2.

Next, a Cartesian coordinate system, $\{s_1^{(\alpha)} \quad s_2^{(\alpha)} \quad s_3^{(\alpha)}\}$, is attached at the centre of mass, $C^{(\alpha)}$, along with the vector basis, $\boldsymbol{e}^{(\alpha)}(t) = \left(\boldsymbol{e}_1^{(\alpha)}(t) \quad \boldsymbol{e}_2^{(\alpha)}(t) \quad \boldsymbol{e}_3^{(\alpha)}(t)\right)$, to each body-$\alpha$. Beginning from the outer component of the system and heading inwards, toward the rotor, body numbers are assigned starting with $\alpha = 1$ for the boat itself.

The translation of body-α with respect to an inertial frame perspective, is designated as $r_C^{(\alpha)}(t)$, expressed using "*x*" as the preferred symbol to designate inertial coordinates,

$$\boldsymbol{r}_C^{(\alpha)}(t) = \boldsymbol{e}^I x_C^{(\alpha)}(t) \tag{1}$$

When expressing the position of body-α relative to another body (α +1), in the system, the *relative position vector* is defined as below, with "*s"* as the symbol.

$$\boldsymbol{s}_C^{(\alpha+1/\alpha)}(t) = \boldsymbol{e}^{(\alpha)}(t)s_C^{(\alpha+1/\alpha)}(t) \tag{2}$$

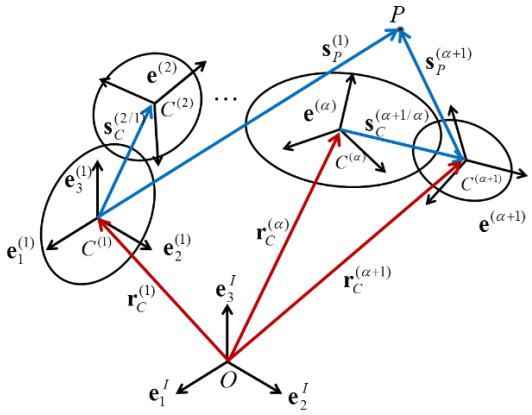

Figure 2: Visual representation of the utilized notation for the kinematics of the system.

The attitude (orientation/rotation) of $\boldsymbol{e}^{(\alpha)}(t)$ measured from $\boldsymbol{e}^I$ is expressed by a $3x3$ rotation matrix $R^{(\alpha)}(t)$ - a member of the $SO(3)$, as,

$$\boldsymbol{e}^{(\alpha)}(t) = \boldsymbol{e}^I R^{(\alpha)}(t) \tag{3}$$

Eqn. (4) describes the orientation of body-(α+1) with respect to body-α,

$$\boldsymbol{e}^{(\alpha+1)}(t) = \boldsymbol{e}^{(\alpha)}(t)R^{(\alpha+1/\alpha)}(t) \tag{4}$$

If the orientation of the $\boldsymbol{e}^{(\alpha+1)}(t)$ body is desired with respect to the inertial frame, Eqn. (3) can be substituted into Eqn. (4) as follows:

$$\boldsymbol{e}^{(\alpha+1)}(t) = \boldsymbol{e}^{\boldsymbol{I}} R^{(\alpha)}(t)R^{(\alpha+1/\alpha)}(t) = \boldsymbol{e}^{\boldsymbol{I}} R^{(\alpha+1)}(t) \tag{5}$$

Since the frames are related through rotation matrices, the inverse of the above Eqns. (3-5) exist, where $R^{-1}(t) = R^T(t)$.

To describe both the translation and orientation of a moving frame compactly, the $4x4$ relative frame connection matrix $E^{(\alpha)}(t)$ of body-α can be defined as follows,

$$\begin{pmatrix}\boldsymbol{e}^{(\alpha)}(t) & \boldsymbol{r}_C^{(\alpha)}(t)\end{pmatrix} = \begin{pmatrix}\boldsymbol{e}^I & 0\end{pmatrix}E^{(\alpha)}(t) = \begin{pmatrix}\boldsymbol{e}^I & 0\end{pmatrix}\begin{bmatrix}R^{(\alpha)}(t) & x_C^{(\alpha)}(t)\\ 0^T & 1\end{bmatrix} \tag{6}$$

These structures were used by Denavit and Hartig as homogenous transformations [4]. However, by recognizing that they are members of $SE(3)$, the MFM is able to extract the full power of such transformations (i.e.: variational methods), as shown in this paper. First, however, the reader is briefly reminded that the notation for 2D and 3D dynamics is the same and this work is conducted by undergraduate students.

Continuing, the relative frame connection matrix is expressed for body-(α+1) with respect to body-α,

$$\left(\boldsymbol{e}^{(\alpha+1)}(t) \quad \boldsymbol{r}_C^{(\alpha+1)}(t)\right) = \left(\boldsymbol{e}^{(\alpha+1/\alpha)} \quad \boldsymbol{r}_C^{(\alpha)}(t)\right)\begin{bmatrix} R^{(\alpha+1/\alpha)}(t) & s_C^{(\alpha)}(t) \\ 0^T & 1 \end{bmatrix} \tag{7}$$

with $0^T = [0 \quad 0 \quad 0]$.

The following recursive relation exists for the relative frame connection matrices,

$$E^{(\alpha+1)}(t) = E^{(\alpha)}(t)E^{(\alpha+1/\alpha)}(t) \tag{8}$$

Ship Kinematics

Eqn. (9) presents the ship frame connection matrix which groups the frame rotation and translation from the origin,

$$\begin{gathered} \left(\boldsymbol{e}^{(1)}(t) \quad \boldsymbol{r}_C^{(1)}(t)\right) = (\boldsymbol{e}^I \quad 0)\begin{bmatrix} R^{(1)}(t) & x_C^{(1)}(t) \\ 0^T & 1 \end{bmatrix} \\ rotation\colon \boldsymbol{e}^{(1)}(t) = \boldsymbol{e}^I R^{(1)}(t) \\ translation\colon \boldsymbol{r}_C^{(1)}(t) = \boldsymbol{e}^I x_C^{(1)}(t) \end{gathered} \tag{9}$$

From this compact form, the rotation of the frame and its location can be readily extracted.

The inverse- and rate of change of the ships frame connection matrix are expressed as,

$$\left(E^{(1)}(t)\right)^{-1} = \begin{bmatrix} \left(R^{(1)}(t)\right)^T & -\left(R^{(1)}(t)\right)^T x_C^{(1)}(t) \\ 0^T & 1 \end{bmatrix}, \tag{10}$$

$$\dot{E}^{(1)}(t) = \begin{bmatrix} \dot{R}^{(1)}(t) & \dot{x}_C^{(1)}(t) \\ 0^T & 0 \end{bmatrix}. \tag{11}$$

To obtain the velocity and angular velocity vectors, the time derivative of Eqn. (9) is taken and expressed with the ship's moving frame using the inverse of Eqn. (9),

$$\left(\dot{\boldsymbol{e}}^{(1)}(t) \quad \dot{\boldsymbol{r}}_C^{(1)}(t)\right) = \left(\boldsymbol{e}^{(1)} \quad \boldsymbol{r}_C^{(1)}(t)\right)\Omega^{(1)}(t), \tag{12}$$

where the $4x4$-time rate of the ship frame connection matrix is expressed as,

$$\Omega^{(1)}(t) = \left(E^{(1)}(t)\right)^{-1}\dot{E}^{(1)}(t). \tag{13}$$

The matrix $\Omega^{(1)}(t)$ explicitly stated below, contains the angular velocity and translational velocity

information with respect to the ship coordinate frame,

$$\Omega^{(1)}(t) = \begin{bmatrix} \overleftrightarrow{\omega^{(1)}(t)} & \left(R^{(1)}(t)\right)^T \dot{x}_C^{(1)}(t) \\ 0^T & 0 \end{bmatrix}. \tag{14}$$

The upper left sub-matrix is the angular velocity matrix,

$$\overleftrightarrow{\omega^{(1)}(t)} = \left(R^{(1)}(t)\right)^T \dot{R}^{(1)}(t), \tag{15}$$

which expresses the time-rate of the ship coordinate frame with respect to its own frame,

$$\dot{\boldsymbol{e}}^{(1)}(t) = \boldsymbol{e}^{(1)}(t)\overleftrightarrow{\omega^{(1)}(t)}. \tag{16}$$

From $\overleftrightarrow{\omega^{(1)}(t)}$, the angular velocity components can be obtained,

$$\boldsymbol{\omega}^{(1)}(t) = \boldsymbol{e}^{(1)}(t)\omega^{(1)}(t) = \begin{bmatrix} \omega_1^{(1)}(t) \\ \omega_2^{(1)}(t) \\ \omega_3^{(1)}(t) \end{bmatrix}. \tag{17}$$

The upper right of $\Omega^{(1)}(t)$ contains the velocity vector of the ship, but it is preferred to write it with respect to the inertial frame so that the forces in the kinetics section to follow can be expressed in the inertial frame as well. Thus, the velocity vector can be expressed as,

$$\dot{\boldsymbol{r}}_C^{(1)}(t) = \boldsymbol{e}^I x_C^{(1)}(t). \tag{18}$$

Gimbal Kinematics

It is assumed that the gimbal has a centre of mass that coincides with the axis of rotation. It will also be assumed that both the gyroscopes are co-located such that $\boldsymbol{s}_C^{(2/1)} = \boldsymbol{s}_C^{(4/1)}$ (the MFM does not require this assumption; the numerical skills of undergraduate students does; this very issue beckons that more research is possible).

In the following, β is used to represent 2 and 4, it is not to be considered as a tentorial quantity, nor mathematical necessity; it is used to shorten the presentation in this paper enabling the listing of two specific equations. The relative position vectors for the two (now co-located) gimbals on the ship can thus be expressed as follows,

$$\boldsymbol{s}_C^{(\beta/1)} = \boldsymbol{e}^{(1)}(t)s_C^{(\beta/1)} = \boldsymbol{e}^{(1)}(t)\begin{bmatrix} h_1^{(\beta/1)} \\ h_2^{(\beta/1)} \\ h_3^{(\beta/1)} \end{bmatrix}. \tag{19}$$

Since the gimbals are precessing around a single axis, specifically the $\boldsymbol{e}_2^{(2)}(t)$ and $\boldsymbol{e}_2^{(4)}(t)$ axes. The relation between the ship and gimbal frames can be expressed by an elementary rotation matrix,

$$\boldsymbol{e}^{(\beta)}(t) = \boldsymbol{e}^{(1)}(t)R^{(\beta/1)}(t). \tag{20}$$

The above rotation matrix can be expressed as follows, where the angle $\phi^{(\beta)}$ represents the precession of each gimbal,

$$R^{(\beta/1)}(t) = R^{(\beta/1)}\left(\phi^{(\beta)}\right) = \begin{bmatrix} \cos\left(\phi^{(\beta)}\right) & 0 & \sin\left(\phi^{(\beta)}\right) \\ 0 & 1 & 0 \\ -\sin\left(\phi^{(\beta)}\right) & 0 & \cos\left(\phi^{(\beta)}\right) \end{bmatrix}. \tag{21}$$

The relative gimbal connection matrix can now be assembled,

$$\left(\boldsymbol{e}^{(\beta)}(t) \quad \boldsymbol{r}_C^{(\beta)}(t)\right) = \left(\boldsymbol{e}^{(1)}(t) \quad \boldsymbol{r}_C^{(1)}(t)\right)\begin{bmatrix} R^{(\beta/1)}(t) & s_C^{(\beta/1)} \\ 0^T & 1 \end{bmatrix} = \left(\boldsymbol{e}^{(1)}(t) \quad \boldsymbol{r}_C^{(1)}(t)\right)E^{(\beta/1)}(t). \tag{22}$$

Following the same approach as for Eqn. (9) for the ship, one obtains the following equations for the frame connection of the gimbals,

$$\boldsymbol{e}^{(\beta)}(t) = \boldsymbol{e}^{(1)}(t)R^{(\beta/1)}(t), \tag{23}$$

$$\boldsymbol{r}_C^{(\beta)}(t) = \boldsymbol{r}_C^{(1)}(t) + \boldsymbol{e}^{(1)}(t)s_C^{(\beta/1)}. \tag{24}$$

As a reminder, β implies 2 or 4 and represents the precession of either structure from the boat frame (frame 1).

The above expression in Eqn. (22) can also be written with respect to the inertial frame,

$$\left(\boldsymbol{e}^{(\beta)}(t) \quad \boldsymbol{r}_C^{(\beta)}(t)\right) = (\boldsymbol{e}^{I} \quad 0)E^{(\beta)}(t) = (\boldsymbol{e}^{I} \quad 0)E^{(1)}(t)E^{(\beta/1)}(t). \tag{25}$$

The inverse- and rate of change of the gimbals frame connection matrix is, respectively, expressed as,

$$\left(E^{(\beta)}(t)\right)^{-1} = \begin{bmatrix} \left(R^{(\beta/1)}(t)\right)^T\left(R^{(1)}(t)\right)^T & -\left(R^{(\beta/1)}(t)\right)^T\left(R^{(1)}(t)\right)^T\left(R^{(1)}(t)s_C^{(\beta/1)} + x_C^{(1)}(t)\right) \\ 0^T & 1 \end{bmatrix}, \tag{26}$$

$$\dot{E}^{(\beta)}(t) = \begin{bmatrix} \dot{R}^{(1)}(t)R^{(\beta/1)}(t) + R^{(1)}(t)\dot{R}^{(\beta/1)}(t) & \dot{R}^{(1)}(t)s_C^{(\beta/1)} + \dot{x}_C^{(1)}(t) \\ 0^T & 0 \end{bmatrix}. \tag{27}$$

To obtain the velocity and angular velocity vectors for the gimbals, previous work [4-5] shows that the time derivative of the above is taken and expressed with the gimbal's moving frame using the inverse of Eqn. (25),

$$\left(\dot{\boldsymbol{e}}^{(\beta)}(t) \quad \dot{\boldsymbol{r}}_C^{(\beta)}(t)\right) = \left(\boldsymbol{e}^{(\beta)}(t) \quad \boldsymbol{r}_C^{(\beta)}(t)\right)\Omega^{(\beta)}(t), \tag{28}$$

where the $4x4$ time rate of the gimbals frame connection matrix is expressed as,

$$\Omega^{(\beta)}(t) = \left(E^{(\beta)}(t)\right)^{-1} \dot{E}^{(\beta)}(t). \tag{29}$$

The matrix $\Omega^{(\beta)}(t)$ explicitly stated below, contains the angular velocity of the gimbal, expressed in the same gimbal coordinate frame,

$$\Omega^{(\beta)}(t) = \begin{bmatrix} \left(\left(R^{(\beta/1)}(t)\right)^T \overleftrightarrow{\omega^{(1)}(t)} R^{(\beta/1)}(t) + \overleftrightarrow{\omega^{(\beta/1)}(t)}\right) & \left(R^{(\beta/1)}(t)\right)^T \left(\overleftrightarrow{\omega^{(1)}(t)} s_C^{(\beta/1)} + \left(R^{(1)}(t)\right)^T \dot{x}_C^{(1)}(t)\right) \\ 0^T & 0 \end{bmatrix}. \tag{30}$$

The angular velocity vectors for the two gimbals can be obtained from the first column as,

$$\overleftrightarrow{\omega^{(\beta)}(t)} = \left(R^{(\beta/1)}(t)\right)^T \overleftrightarrow{\omega^{(1)}(t)} R^{(\beta/1)}(t) + \overleftrightarrow{\omega^{(\beta/1)}(t)}. \tag{31}$$

Even though the equation above is correct, the term should be modified so that the omega appears at the end to facilitate the use of generalized coordinates. It is straightforward to show that the following is true [4],

$$\left(R^{(\beta/1)}(t)\right)^T \overleftrightarrow{\omega^{(1)}(t)} R^{(\beta/1)}(t) = \overleftrightarrow{\left(R^{(\beta/1)}(t)\right)^T \omega^{(1)}(t)}. \tag{32}$$

Eqn. (31) is thus simplified to,

$$\omega^{(\beta)}(t) = \left(R^{(\beta/1)}(t)\right)^T \omega^{(1)}(t) + \omega^{(\beta/1)}(t). \tag{33}$$

Above, the last term will become one of the generalized coordinates.

The velocity vector component can be obtained from the second column. Expressing the component with respect to the inertial frame results,

$$\dot{\boldsymbol{r}}_C^{(\beta)}(t) = \boldsymbol{e}^I \dot{x}_C^{(1)}(t). \tag{34}$$

Rotor Kinematics

Similar to the ship and the gimbals, the rotors relative frame connection matrix and velocity and angular velocity vectors have to be obtained. The kinematics for the rotor are found as with the gimbal. It will be assumed that the centre of mass of each rotor coincides with the centre of mass of their respective gimbal, thus the relative position vector of the rotors with respect to the gimbals will be zero.

In the following, "Σ" is used to represent "3" and "5" respectively for the left and right rotor,

$$\boldsymbol{s}_C^{(\Sigma/\beta)} = \boldsymbol{e}^{(\beta)}(t) s_C^{(\Sigma/\beta)} = \boldsymbol{e}^{(\beta)}(t) \begin{bmatrix} 0 \\ 0 \\ 0 \end{bmatrix}. \tag{35}$$

Note that this is not standard index notation. The following associations, made to reduce publication space, are essential;

$$left\ rotor: \Sigma = 3, \beta = 2$$
$$right\ rotor: \Sigma = 5, \beta = 4$$

Since the rotors are rotating around a single axis, specifically the $\boldsymbol{e}_3^{(3)}(t)$ and the $\boldsymbol{e}_3^{(5)}(t)$ axes, the relation between the gimbal and rotor frames can be expressed by an elementary rotation matrix,

$$R^{(\Sigma/\beta)}(t) = R^{(\Sigma/\beta)}\left(\psi^{(\Sigma)}\right) = \begin{bmatrix} \cos\left(\psi^{(\Sigma)}\right) & -\sin\left(\psi^{(\Sigma)}\right) & 0 \\ \sin\left(\psi^{(\Sigma)}\right) & \cos\left(\psi^{(\Sigma)}\right) & 0 \\ 0 & 0 & 1 \end{bmatrix}. \tag{36}$$

The rotor frame connection matrix can now be assembled,

$$\left(\boldsymbol{e}^{(\Sigma)}(t) \quad \boldsymbol{r}_C^{(\Sigma)}(t)\right) = \left(\boldsymbol{e}^{(\beta)}(t) \quad \boldsymbol{r}_C^{(\beta)}(t)\right)\begin{bmatrix} R^{(\Sigma/\beta)}(t) & 0 \\ 0^T & 1 \end{bmatrix} = \left(\boldsymbol{e}^{(\beta)}(t) \quad \boldsymbol{r}_C^{(\beta)}(t)\right)E^{(\Sigma/\beta)}(t). \tag{37}$$

Following the same method as for Eqn. (9), for the ship, the following equations are obtained for the frame connection and translation of the rotors,

$$\boldsymbol{e}^{(\Sigma)}(t) = \boldsymbol{e}^{(\beta)}(t)R^{(\Sigma/\beta)}(t), \tag{38}$$

$$\boldsymbol{r}_C^{(\Sigma)}(t) = \boldsymbol{r}_C^{(\beta)}(t). \tag{39}$$

Eqn. (37) can also be written with respect to the inertial frame,

$$\left(\boldsymbol{e}^{(\Sigma)}(t) \quad \boldsymbol{r}_C^{(\Sigma)}(t)\right) = (\boldsymbol{e}^{I} \quad 0)E^{(\Sigma)}(t) = (\boldsymbol{e}^{I} \quad 0)E^{(\Sigma)}(t)E^{(\Sigma/\beta)}(t). \tag{40}$$

The inverse and the rate of change of the rotors frame connection matrix is needed to calculate $\Omega^{(3)}(t)$ and $\Omega^{(5)}(t)$. The inverse and the rate of change of the rotors frame connection matrices is, respectively, expressed as,

$$\left(E^{(\Sigma)}(t)\right)^{-1} = \begin{bmatrix} \left(R^{(\Sigma/\beta)}(t)\right)^T \left(R^{(\beta/1)}(t)\right)^T \left(R^{(1)}(t)\right)^T & -\left(R^{(\Sigma/\beta)}(t)\right)^T \left(R^{(\beta/1)}(t)\right)^T \left(R^{(1)}(t)\right)^T x_C^{(1)}(t) \\ 0^T & 1 \end{bmatrix}, \tag{41}$$

$$\dot{E}^{(\beta)}(t) = \begin{bmatrix} \dot{R}^{(1)}(t)R^{(\beta/1)}(t)R^{(\Sigma/\beta)}(t) + R^{(1)}(t)\dot{R}^{(\beta/1)}(t)R^{(\Sigma/\beta)}(t) + R^{(1)}(t)R^{(\beta/1)}(t)\dot{R}^{(\Sigma/\beta)}(t) & \dot{x}_C^{(1)}(t) \\ 0^T & 0 \end{bmatrix}. \tag{42}$$

To obtain the velocity and angular velocity vectors for the rotors, the time derivative of the above is taken and expressed with the rotor's moving frame using the inverse of Eqn. (40),

$$\left(\dot{\boldsymbol{e}}^{(\Sigma)}(t) \quad \dot{\boldsymbol{r}}_C^{(\Sigma)}(t)\right) = \left(\boldsymbol{e}^{(\Sigma)}(t) \quad \boldsymbol{r}_C^{(\Sigma)}(t)\right)\Omega^{(\Sigma)}(t), \tag{43}$$

where the $4x4$ time rate of the rotors frame connection matrix is expressed as,

$$\Omega^{(\Sigma)}(t) = \left(E^{(\Sigma)}(t)\right)^{-1} \dot{E}^{(\Sigma)}(t). \tag{44}$$

The velocity of the rotors is already known to be the same as the velocities of the gimbals. Therefore, the angular velocity of the rotors is the only focus. The angular velocity vectors for the two rotors can be obtained from the first column of $\Omega^{(\Sigma)}(t)$,

$$\overleftrightarrow{\omega^{(\Sigma)}(t)} = \left(R^{(\Sigma/1)}(t)\right)^T \overleftrightarrow{\omega^{(1)}(t)} R^{(\Sigma/1)}(t) + \left(R^{(\Sigma/\beta)}(t)\right)^T \overleftrightarrow{\omega^{(\beta/1)}(t)} R^{(\Sigma/\beta)}(t) + \overleftrightarrow{\omega^{(\Sigma/\beta)}(t)}. \tag{45}$$

Even though the equation above is correct, the term must be modified so that the angular velocity components appear at the end, in order to exploit generalized coordinates. One can easily show that the following is true,

$$\left(R^{(\Sigma/1)}(t)\right)^T \overleftrightarrow{\omega^{(1)}(t)} R^{(\Sigma/1)}(t) = \overleftrightarrow{\left(R^{(\Sigma/1)}(t)\right)^T \omega^{(1)}(t)}, \tag{46}$$

$$\left(R^{(\Sigma/\beta)}(t)\right)^T \overleftrightarrow{\omega^{(\beta/1)}(t)} R^{(\Sigma/\beta)}(t) = \overleftrightarrow{\left(R^{(\Sigma/\beta)}(t)\right)^T \omega^{(\beta/1)}(t)}. \tag{47}$$

$$\omega^{(\beta)}(t) = \left(R^{(\beta/1)}(t)\right)^T \omega^{(1)}(t) + \omega^{(\beta/1)}(t). \tag{33}$$

Thus, eqn. (45) is simplified to,

$$\omega^{(\Sigma)}(t) = \left(R^{(\Sigma/1)}(t)\right)^T \omega^{(1)}(t) + \left(R^{(\Sigma/\beta)}(t)\right)^T \omega^{(\beta/1)}(t) + \omega^{(\Sigma/\beta)}(t). \tag{48}$$

The velocity vector components can be obtained from the second column. Expressing the component with respect to the inertial frame,

$$\dot{\boldsymbol{r}}_C^{(\Sigma)}(t) = \boldsymbol{e}^I \dot{x}_C^{(\beta)}(t). \tag{49}$$

B-Matrix

The system consists of five major components, or five moving frames, each with a corresponding velocity and angular velocity vector. These are, one boat, two gimbals and two disks. The components can collectively be expressed in a $30x1$ column matrix $\{\dot{X}(t)\}$, referred to as the generalized velocities.

The generalized velocities can be more simply expressed by the set of independent velocities, the essential generalized velocities, which are assembled in a $30x1$ column matrix $\{\dot{X}^*(t)\}$,

$$\{\dot{X}(t)\} = \begin{Bmatrix} \dot{x}_C^{(1)}(t) \\ \omega^{(1)}(t) \\ \dot{x}_C^{(2)}(t) \\ \omega^{(2)}(t) \\ \dot{x}_C^{(3)}(t) \\ \omega^{(3)}(t) \\ \dot{x}_C^{(4)}(t) \\ \omega^{(4)}(t) \\ \dot{x}_C^{(5)}(t) \\ \omega^{(5)}(t) \end{Bmatrix}, \qquad \{\dot{X}^*(t)\} = \begin{Bmatrix} \dot{x}_C^{(1)}(t) \\ \omega^{(1)}(t) \\ \dot{\phi}^{(2)} \\ \dot{\phi}^{(4)} \\ \dot{\psi}^{(3)} \\ \dot{\psi}^{(5)} \end{Bmatrix}. \tag{50}$$

The generalized velocities are linearly related to the essential generalized velocities using the $[B(t)]$ matrix,

$$\{\dot{X}(t)\} = [B(t)]\{\dot{X}^*(t)\}. \tag{51}$$

$[B(t)]$ is a $30x10$ matrix assembled from the velocity and angular velocity vectors derived in the kinematics section. However, before deriving the B-matrix, another assumption must be made; the distance from the centre of the boat to the centre of the gimbals is so short that it will be set equal to 0 (but beckons future research). This simplifies the expression for the velocity vector component of the gimbal as shown in the B-matrix below,

$$\begin{Bmatrix} \dot{x}_C^{(1)}(t) \\ \omega^{(1)}(t) \\ \dot{x}_C^{(2)}(t) \\ \omega^{(2)}(t) \\ \dot{x}_C^{(3)}(t) \\ \omega^{(3)}(t) \\ \dot{x}_C^{(4)}(t) \\ \omega^{(4)}(t) \\ \dot{x}_C^{(5)}(t) \\ \omega^{(5)}(t) \end{Bmatrix} = \begin{bmatrix} I_3 & 0_3 & 0_1 & 0_1 & 0_1 & 0_1 \\ 0_3 & I_3 & 0_1 & 0_1 & 0_1 & 0_1 \\ I_3 & 0_3 & 0_1 & 0_1 & 0_1 & 0_1 \\ 0_3 & \left(R^{(2/1)}(t)\right)^T & e_2 & 0_1 & 0_1 & 0_1 \\ I_3 & 0_3 & 0_1 & 0_1 & 0_1 & 0_1 \\ 0_3 & \left(R^{(3/1)}(t)\right)^T & \left(R^{(3/2)}(t)\right)^T e_2 & 0_1 & e_3 & 0_1 \\ I_3 & 0_3 & 0_1 & 0_1 & 0_1 & 0_1 \\ 0_3 & \left(R^{(4/1)}(t)\right)^T & 0_1 & e_2 & 0_1 & 0_1 \\ I_3 & 0_3 & 0_1 & 0_1 & 0_1 & 0_1 \\ 0_3 & \left(R^{(5/1)}(t)\right)^T & 0_1 & \left(R^{(5/4)}(t)\right)^T e_2 & 0_1 & e_3 \end{bmatrix} = \begin{Bmatrix} \dot{x}_C^{(1)}(t) \\ \omega^{(1)}(t) \\ \dot{\phi}^{(2)} \\ \dot{\phi}^{(4)} \\ \dot{\psi}^{(3)} \\ \dot{\psi}^{(5)} \end{Bmatrix}. \tag{52}$$

In the above,

$$0_1 = \begin{bmatrix} 0 \\ 0 \\ 0 \end{bmatrix}, \qquad 0_3 = \begin{bmatrix} 0 & 0 & 0 \\ 0 & 0 & 0 \\ 0 & 0 & 0 \end{bmatrix}, \qquad I_3 = \begin{bmatrix} 1 & 0 & 0 \\ 0 & 1 & 0 \\ 0 & 0 & 1 \end{bmatrix}. \tag{53}$$

The derivation of the B-matrix concludes the kinematics of the system shown in Fig. 1.

Kinetics

In this section, the equations of motion for the system will be derived using the Principal of Virtual Work obtained from Hamilton's Principle. To derive the principle of virtual work, the Lagrangian $\hat{L}$ is defined as the difference between the kinetic energy K and the potential energy K,

$$\hat{L} = K - U \tag{54}$$

The kinetic energy consists of both translational and rotational energy with respect to the centre of mass of each of the components. To define the total kinetic energy of the system, expressions for the linear momentum, $\boldsymbol{L}_C^{(\alpha)}$, and angular momentum, $\boldsymbol{H}_C^{(\alpha)}$, are needed,

$$\boldsymbol{L}_C^{(\alpha)} = \boldsymbol{e}^I L_C^{(\alpha)} = \boldsymbol{e}^I m^{(\alpha)} \dot{x}_C^{(\alpha)}, \tag{55}$$

$$\boldsymbol{H}_C^{(\alpha)} = \boldsymbol{e}^{(\alpha)} H_C^{(\alpha)} = \boldsymbol{e}^{(\alpha)} J_C^{(\alpha)} \dot{x}_C^{(\alpha)}. \tag{56}$$

The total kinetic energy can be more compactly expressed in matrix form as,

$$K = \frac{1}{2}\{\dot{X}(t)\}^T \{H(t)\} = \frac{1}{2}\{\dot{X}(t)\}^T [M]\{\dot{X}(t)\}, \tag{57}$$

where $\{H(t)\}$, the generalized momenta, contain both linear and angular momentum (note that, henceforth, we must now undo the dual notation for the left and right gyro-systems and return to specificity),

$$\{H(t)\} = \begin{Bmatrix} L_C^{(1)}(t) \\ H_C^{(1)}(t) \\ L_C^{(2)}(t) \\ H_C^{(2)}(t) \\ L_C^{(3)}(t) \\ H_C^{(3)}(t) \\ L_C^{(4)}(t) \\ H_C^{(4)}(t) \\ L_C^{(5)}(t) \\ H_C^{(5)}(t) \end{Bmatrix} = [M]\{\dot{X}(t)\}, \tag{58}$$

and $[M]$, the generalized mass matrix, is a diagonal matrix containing both masses and moments of inertia of the bodies in the system,

$$[M] = \begin{bmatrix} m^{(1)}I_3 & 0_3 & 0_3 & 0_3 & 0_3 & 0_3 & 0_3 & 0_3 & 0_3 & 0_3 \\ 0_3 & J_C^{(1)} & 0_3 & 0_3 & 0_3 & 0_3 & 0_3 & 0_3 & 0_3 & 0_3 \\ 0_3 & 0_3 & m^{(2)}I_3 & 0_3 & 0_3 & 0_3 & 0_3 & 0_3 & 0_3 & 0_3 \\ 0_3 & 0_3 & 0_3 & J_C^{(2)} & 0_3 & 0_3 & 0_3 & 0_3 & 0_3 & 0_3 \\ 0_3 & 0_3 & 0_3 & 0_3 & m^{(3)}I_3 & 0_3 & 0_3 & 0_3 & 0_3 & 0_3 \\ 0_3 & 0_3 & 0_3 & 0_3 & 0_3 & J_C^{(3)} & 0_3 & 0_3 & 0_3 & 0_3 \\ 0_3 & 0_3 & 0_3 & 0_3 & 0_3 & 0_3 & m^{(4)}I_3 & 0_3 & 0_3 & 0_3 \\ 0_3 & 0_3 & 0_3 & 0_3 & 0_3 & 0_3 & 0_3 & J_C^{(4)} & 0_3 & 0_3 \\ 0_3 & 0_3 & 0_3 & 0_3 & 0_3 & 0_3 & 0_3 & 0_3 & m^{(5)}I_3 & 0_3 \\ 0_3 & 0_3 & 0_3 & 0_3 & 0_3 & 0_3 & 0_3 & 0_3 & 0_3 & J_C^{(5)} \end{bmatrix}. \quad (59)$$

The above is simply a structure from which the equations of motion will be extracted. For the moments of inertia above, the coordinate systems are located in the centre of mass of each body and coincide with the principal axes, resulting in diagonal $J_C^{(\alpha)}$ matrices.

The potential energy U of each body is due to gravitational acceleration,

$$U^{(\alpha)} = m^{(\alpha)} g x_C^{(\alpha)}. \quad (60)$$

To take the variation of the Lagrangian, the variation of the generalized velocities and displacements needs to be obtained. Murakami [5] defines variation of a body- α frame connection matrix as,

$$\delta\Pi^{(\alpha)} = \begin{bmatrix} \overleftrightarrow{\delta\pi^{(\alpha)}(t)} & R^{(\alpha)}(t)\delta x_C^{(\alpha)}(t) \\ 0_{1x2}^T & 0 \end{bmatrix}. \quad (61)$$

The virtual rotational displacements, $\overleftrightarrow{\delta\pi^{(\alpha)}(t)}$, is also defined as,

$$\overleftrightarrow{\delta\pi^{(\alpha)}(t)} = \left(R^{(\alpha)}(t)\right)^T \delta R^{(\alpha)}(t), \quad (62)$$

$$\delta\boldsymbol{\pi}^{(\alpha)}(t) = \boldsymbol{e}^{(\alpha)}\delta\pi^{(\alpha)}(t). \quad (63)$$

As an aside, π does not exist, it simply exists in its representation of the product form of $\delta\pi$, which accounts for the variations of the angular velocities.

The virtual generalized displacements are assembled in a column matrix $\{\delta\tilde{X}\}$,

$$\{\delta\tilde{X}\} = \begin{Bmatrix} \delta x_C^{(1)} \\ \delta\pi_C^{(1)} \\ \delta x_C^{(2)} \\ \delta\pi_C^{(2)} \\ \delta x_C^{(3)} \\ \delta\pi_C^{(3)} \\ \delta x_C^{(4)} \\ \delta\pi_C^{(4)} \\ \delta x_C^{(5)} \\ \delta\pi_C^{(5)} \end{Bmatrix}. \tag{64}$$

Imposing the commutativity of time differentiation, the d/dt operator, and the variation of the frame, the δ operator, results in the variation of the generalized angular velocities and velocities,

$$\delta\omega^{(\alpha)}(t) = \frac{d}{dt}\delta\pi^{(\alpha)}(t) + \overleftrightarrow{\omega^{(\alpha)}(t)}\delta\pi^{(\alpha)}(t), \tag{65}$$

$$\frac{d}{dt}\delta x_C^{(\alpha)}(t) = \delta\dot{x}_C^{(\alpha)}(t). \tag{66}$$

Eqn. (65) is a powerful formula and represents a restriction on the variation of the angular velocity.

Placing the above equations in matrix form for use in the variation of the Lagrangian results in,

$$\{\delta\dot{X}\} = \{\delta\dot{\tilde{X}}\} + [D]\{\delta\tilde{X}\}, \tag{67}$$

where the skew symmetric matrix $[D]$ is expressed as,

$$[D] = \begin{bmatrix} 0_3 & 0_3 & 0_3 & 0_3 & 0_3 & 0_3 & 0_3 & 0_3 & 0_3 & 0_3 \\ 0_3 & \omega^{(1)}(t) & 0_3 & 0_3 & 0_3 & 0_3 & 0_3 & 0_3 & 0_3 & 0_3 \\ 0_3 & 0_3 & 0_3 & 0_3 & 0_3 & 0_3 & 0_3 & 0_3 & 0_3 & 0_3 \\ 0_3 & 0_3 & 0_3 & \omega^{(2)}(t) & 0_3 & 0_3 & 0_3 & 0_3 & 0_3 & 0_3 \\ 0_3 & 0_3 & 0_3 & 0_3 & 0_3 & 0_3 & 0_3 & 0_3 & 0_3 & 0_3 \\ 0_3 & 0_3 & 0_3 & 0_3 & 0_3 & \omega^{(3)}(t) & 0_3 & 0_3 & 0_3 & 0_3 \\ 0_3 & 0_3 & 0_3 & 0_3 & 0_3 & 0_3 & 0_3 & 0_3 & 0_3 & 0_3 \\ 0_3 & 0_3 & 0_3 & 0_3 & 0_3 & 0_3 & 0_3 & \omega^{(4)}(t) & 0_3 & 0_3 \\ 0_3 & 0_3 & 0_3 & 0_3 & 0_3 & 0_3 & 0_3 & 0_3 & 0_3 & 0_3 \\ 0_3 & 0_3 & 0_3 & 0_3 & 0_3 & 0_3 & 0_3 & 0_3 & 0_3 & \omega^{(5)}(t) \end{bmatrix} \tag{68}$$

Thus, the variation of the Lagrangian becomes,

$$\delta L = \{\delta \dot{X}\}^T [M]\{\dot{X}\} - \{\delta \tilde{X}\}^T \{G\}, \tag{69}$$

where $\{G\}$ represents the gravitational force,

$$\{G\} = \begin{Bmatrix} m^{(1)} g e_3 \\ 0_1 \\ m^{(2)} g e_3 \\ 0_1 \\ m^{(3)} g e_3 \\ 0_1 \\ m^{(4)} g e_3 \\ 0_1 \\ m^{(5)} g e_3 \\ 0_1 \end{Bmatrix}. \tag{70}$$

The moments and forces acting on the system are those due to ocean waves, while the actuator couples are due to the motors powering the rotor and rocking the gimbal. The actuator couples and forces are factored in due to Newton's third law of action and reaction. The generalized forces, including those due to the gravitational force $\{G\}$, will be expressed by $\{Q\}$. Thus, the virtual work done by the generalized forces is expressed as,

$$\delta W = \{\delta X\}^T \{Q(t)\}, \tag{71}$$

with $\{Q(t)\}$ defined as,

$$\{Q(t)\} = \begin{Bmatrix} F_C^{(1)I}(t) \\ M_C^{(1)}(t) \\ F_C^{(2)I}(t) \\ M_C^{(2)}(t) \\ F_C^{(3)I}(t) \\ M_C^{(3)}(t) \\ F_C^{(4)I}(t) \\ M_C^{(4)}(t) \\ F_C^{(5)I}(t) \\ M_C^{(5)I}(t) \end{Bmatrix} = \begin{Bmatrix} F^{(w)I}(t) + F_b^I - m^{(1)} g e_3 \\ M^{(w)}(t) \\ -m^{(2)} g e_3 \\ -M_m^{(r)}(t) e_3 + M_m^{(g)}(t) e_2 \\ -m^{(3)} g e_3 \\ M_m^{(r)}(t) e_3 \\ -m^{(4)} g e_3 \\ M_m^{(r)}(t) e_3 - M_m^{(g)}(t) e_2 \\ -m^{(5)} g e_3 \\ -M_m^{(r)}(t) e_3 \end{Bmatrix}. \tag{72}$$

In the above equation, $F^{(w)I}(t)$ and $M^{(w)}(t)$ are the wave forces and couples acting on the ship, respectively. The constant buoyancy force, F_b^I, can be expressed as,

$$F_b^I = \left(m^{(1)} + m^{(2)} + m^{(3)} + m^{(4)} + m^{(5)}\right) g e_3. \tag{73}$$

The superscript I indicates that the components of the forces are with respect to the inertial frame. The action and reaction couples $M_m^{(r)}(t)$ and $M_m^{(g)}(t)$ are due to the motors operating the rotors and gimbals respectively. The rotors and gimbals are prescribed in opposite directions. Currently, the effect of added mass fluid resistance and drag force is not considered.

Hamilton's principle is now written using Eqns. (69) and (71),

$$\int_{t_0}^{t_1} \left[\left\{ \delta \dot{\tilde{X}} \right\}^T \{H\} + \{\delta \tilde{X}\}^T ([D]^T \{H\} + \{Q(t)\}) \right] dt = 0. \tag{74}$$

Integrating by parts, and noting that the virtual displacements vanish at t_0 and t_1, yields the principle of virtual work that holds for all time,

$$\int_{t_0}^{t_1} \{\delta \tilde{X}\}^T \left[\{\dot{H}(t)\} + [D]\{H\} - \{Q(t)\} \right] dt = 0. \tag{75}$$

The equations of motion can now be derived from the principal of virtual work, shown in Eqn. (75). To simplify the analysis and the number of equations, the essential virtual displacements are obtained,

$$\{\delta q\} = \begin{Bmatrix} \delta x_C^{(1)} \\ \delta \pi^{(1)} \\ \delta \phi^{(2)} \\ \delta \phi^{(4)} \\ \delta \psi^{(3)} \\ \delta \psi^{(5)} \end{Bmatrix}. \tag{76}$$

As done with the generalized velocities in Eqn. (51), a similar relation can be obtained that relates the virtual generalized displacements, $\{\delta \tilde{X}^*\}$, and the essential virtual displacements, $\{\delta q\}$,

$$\{\delta \tilde{X}^*\} = [B]\{\delta q\}. \tag{77}$$

The generalized momenta derived in Eqn. (59), can be written with respect to the essential generalized velocities,

$$\{H(t)\} = [M][B]\{\dot{X}^*\}. \tag{78}$$

Substituting Eqns. (77) and (78) back into the principal of virtual work, results in,

$$\{\delta q(t)\}^T \left(\begin{array}{c} [B(t)]^T[M][B(t)]\{\ddot{X}^*(t)\} \\ +[B(t)]^T\left([M]\left[\dot{B}(t)\right] + [D(t)][M][B(t)]\right)\{\dot{X}^*(t)\} \\ -[B(t)]^T\{Q(t)\} \end{array} \right) = 0 \quad (79)$$

Finally, the general formula for deriving the equations of motion through the use of essential generalized velocities is obtained,

$$[B(t)]^T[M][B(t)]\{\ddot{X}^*(t)\} + [B(t)]^T\left([M]\left[\dot{B}(t)\right] + [D(t)][M][B(t)]\right)\{\dot{X}^*(t)\} - [B(t)]^T\{Q(t)\} = 0 \quad (80)$$

8 Background Theory Hydrodynamics

Natural Period

The natural frequency of an object is the frequency at which a body naturally tends to vibrate if subjected to a disturbance. The natural period is the period of one complete oscillation of a body. In a damped system, such as a ship in water, the excitations will decay and eventually come to a stop, as shown in Fig. 3. This is due to dampening effects from the water.

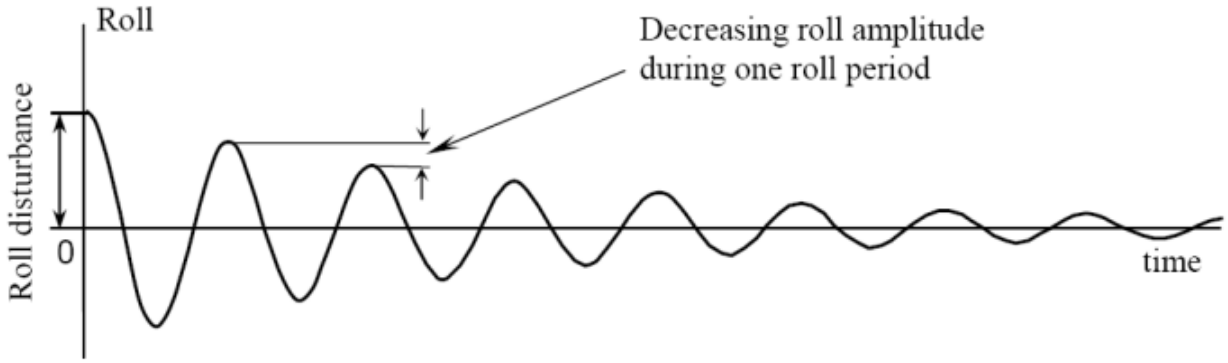

Figure 3: Motion of a damped system [25].

The natural period in rolling motion is defined as,

$$T = \frac{2\pi k}{\sqrt{gGM}} \quad (81)$$

Altering the natural period is often necessary when it comes to rolling motion of a ship or barge. If the vessel has the same natural frequency as a wave spectrum this can lead to great roll angles and amplitude, which can be unfortunate for both cargo and crew.

As equation (81) suggests, the natural period can be altered by changing the metacentric height, GM (Fig. 4), or by changing the radius of gyration, k. The metacentric height is defined as,

$$GM = KB + BM - KG = KB + \frac{I}{\nabla} - KG. \tag{82}$$

Thus, the metacentric height can be altered by changing the centre of gravity (i.e. moving cargo toward the keel) or changing the geometry of the ship, which influences the centre of buoyancy, B (Fig. 4) and the second moment of area, I. The radius of gyration can be changing the mass distribution around the axis of roll, with increased distance from the axis of roll to the mass, leading to an increase in radius of gyration (i.e. moving cargo toward the sides of the ship, in roll and toward the stern and bow, in pitch). Increasing the metacentric height leads to a decrease in natural period and increasing the radius of gyration leads to an increase in natural period.

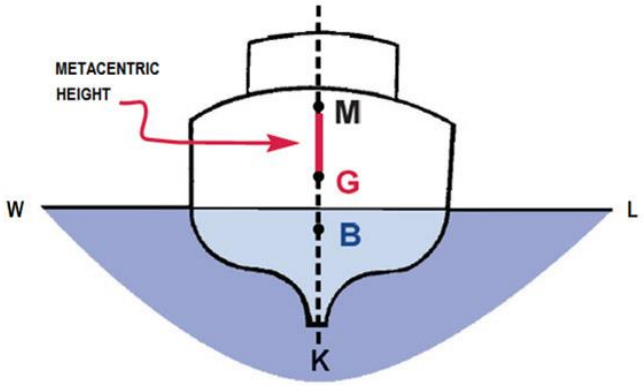

Figure 4: Illustration of metacentric height and centre of buoyancy.

Resonance

Resonance is defined as the phenomenon that occurs when a vibrating system or external force drives a body/system to oscillate with greater amplitude at a specific preferential frequency. At sea, this can happen when waves at a specific frequency influences ships with a given natural frequency, and these to frequencies is close to or equal. This is especially a worrying problem when it comes to roll motion. If resonance does not occur and the natural frequency of the ship is different from the wave frequency, the rolling motion will decrease or remain stable. However, if the natural period of the ship is in coherence with the wave period (Fig. 5), the rolling motion of the ship can increase, which can lead to dangerous situations putting both cargo and crew at risk.

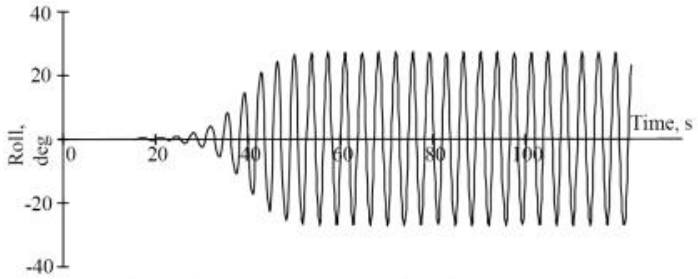

Figure 5: Rolling motion of a ship experiencing resonance [25].

Most dangerous is the so called 2:1 resonance were two pitch wave cycles coincide with one roll

cycle of the system leading to great roll angles. To better understand the phenomenon, 1:1 resonance occurs when one pitch cycle coincides with one roll cycle, meaning that one wave period coincide with one ship roll period. The 1:1 resonance is the exact case for our ship experiments, resulting in problematic roll angles but not as critical angles as the 2:1 resonance phenomenon [26].

8.1 Ship Stabilization Systems

A vessel or barge exposed to wind and waves experience motion in the six degrees of freedom, surge, sway, heave, roll, pitch and yaw. The roll motion is the most critical because it is lightly damped and therefore prone to dynamic magnification in the resonance frequency range. A rolling vessel can also cause crew discomfort which leads to inefficiency, damaged cargo and equipment. Throughout the years, roll motion has been a critical part of vessel design. These rolling effects can be limited by the use of stabilization systems. To guarantee the safety of a vessel, it is important to understand the characteristics of roll motion of the vessel in order to estimate the movement of the vessel. However, due to viscous effects and vortex shedding, these properties can be difficult to predict.

Ship stabilization systems are separated into passive and active systems. Some of the most commonly used systems are listed below.

Passive stabilization systems:
- Bilge keels.
- Trim tabs.
- Passive anti-roll tanks.

Active stabilization systems:
- Rudder stabilization.
- Fins.
- Active anti-roll tanks.
- Gyroscopic stabilization systems.

Some of these systems uses pressure differences, which occurs at speed (i.e. fins, trim tabs). Because the model used in this paper is a stationary barge, these systems will not be discussed. Gyroscopic stabilizers are discussed in Experimental Setup, Part II.

Bilge Keels

Bilge keels (Fig. 6) are the most common used passive ship stabilization system. The bilge keels are fitted in pairs, toward the bottom of the side of the hull, and often run along much of the length of the ship. How the bilge keel effect the roll motion of a vessel depends on bilge radius, length, width, position along the ship, angle, and the size of the vessel [27]. Bilge keels are widely used on different kinds of vessel types. This is because the bilge keels are easily fitted to any kind of vessel, at a low cost. Further, it does not occupy any internal space and does not affect the original hull shape. On the other hand, bilge keels do not contribute as much to roll damping, as active stabilization systems. Therefore, they are often used in combination with other systems. The bilge

keels also effect the hydrodynamic resistance of the vessel in a negative way, hindering forward motion. However, it is not a concern for the model used in this paper.

As proposed by Himeno [28], roll damping can be separated into seven different and separate effects. Three of these effects are due to bilge keels:

1. Normal-force bilge keel damping.
2. Hull-pressure bilge keel damping.
3. Wave bilge keel damping.

Normal-force and hull-pressure damping have been shown to vary approximately linearly with angular velocity [28], thus, larger angular velocities should produce larger effects on the roll damping of the barge. The third effect is due to the additional wave radiation, because of the added bilge keels. However, Himeno [28] concludes that this term is negligible compared to the first and second term. Even though Himeno's paper was published in 1981, it is still the practice used [29].

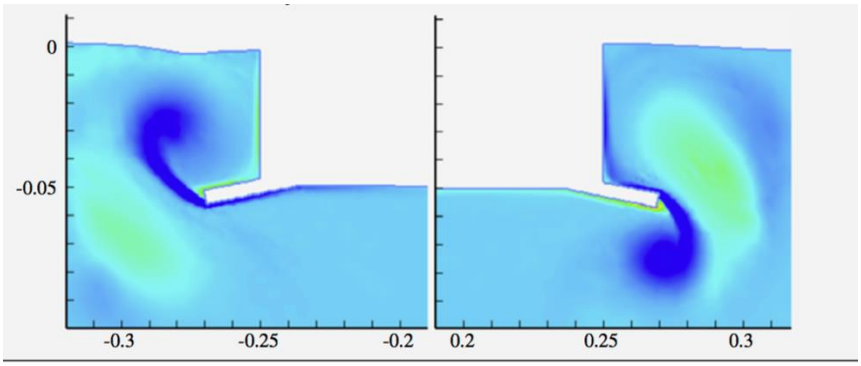

Figure 6: Bilge keels on a rectangular vessel.

Passive Anti-Roll Tanks

Anti-roll tanks dates back to William Froude [30]. Froude installed water chambers in the upper part of a ship to reduce the movement in roll motion. These anti-roll tanks are free surface tanks that are supposed to counteract the roll motion of the ship. As the water moves from one side to the other, inside the chamber, the roll motion of the vessel can be reduced. By changing the level in the chambers, one can control the natural frequency of the tank. Froude's free surface tanks did not receive much attention until the middle of the 20th century when it became widely used in naval vessels. Another type of anti-roll tank is the U-tube tank (Fig. 7), introduced by Frahm in 1910 [31]. The U-tube tank works one the same principles as Froude's anti-roll tank. By moving water from one side of the U-shaped tank to another, a counteracting roll moment is produced. The movement of water is controlled by baffles.

Passive anti-roll tanks have the advantage of high efficiency at no speed. The anti-roll tanks can be placed along the hull or at the upper part of the ship. As they are placed inside the hull, they are not easily damaged. Thus, they do not affect the hydrodynamic drag of the ship. The disadvantage

of these systems are that they take up a large amount of space.

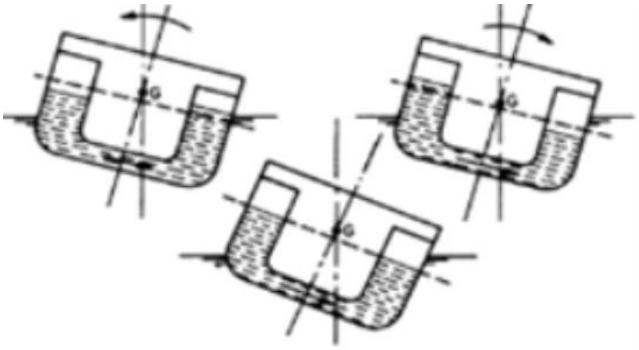

Figure 7: U-tube anti-roll tanks [32].

9 Method

9.1 Experimental Setup: Part I

9.1.1 Scale Model

The scaled model is made according to CAD drawings, provided by AKVA Group, from the keel to main deck. Since this paper studies the hydrodynamic properties of a barge, the scaled model is not built according to the full-scale model from main deck and up. It is preferable to build the scaled model as large as possible, taking into account the limitations imposed by the wave tank. This is due to effects, which are difficult to scale (i.e. viscous effects). The scale used is 27 and is defined as,

$$\lambda = \frac{LOA_F}{LOA_M} \, . \tag{83}$$

The full size barge has a length over all of 50 meters, is 12 meters wide and has a height of 10 meters. Drawings of the scaled model and gyroscope are found in Appendix A.

Before making the scaled model, a solid part is drawn in Creo Parametric. Associated 2D drawings includes general view, projection view and section surface. The model is made from Divinycell, a lightweight, sandwich core material, used for building ship models. The layers of Divinycell is designed by making several datum planes, which are shown in Appendix A. A requirement is that the thickness of the Divinycell must be greater than 40 mm. During the building process, the Divinycell plates are measured with a safety deviation of around 10 millimetres at each side before cutting. The layers of Divinycell are glued together using Relekta glue. Vertical and horizontal pressure are applied for stable conditions during drying. The glue dries for 24 hours before the barge is milled at the machine lab at HVL. The milled model is shown in Fig. 8 The model surface

is brushed with sandpaper and coated with filling four times. At last, the model surface is spray-painted.

Figure 8: Scaled model after milling.

As discussed in the background theory, metacentric height and radius of gyration are important properties, deciding roll motion of a ship. Since the metacentric height depends on these properties, the metacentric height will be scaled by ensuring that the geometry, the mass and the location of mass is scaled correctly. The mass of the model is found from,

$$\Delta_M = \frac{\Delta_F}{\lambda^3}\frac{\rho_M}{\rho_F}, \tag{84}$$

where ρ_M is the density of the fluid surrounding the scaled model and ρ_F is the density of the fluid surrounding the full size barge, in this case the density of fresh water and salt water respectively. The radius of gyration is found by studying plate drawings of the full size barge and calculating the radius of gyration. Since the radius of gyration is a length unit, it can be scaled by λ. When estimating the radius of gyration some simplifications have to be made. The entire hull is divided into steel plates, stiffeners, generators and various equipment. One of the simplifications made is to add transverse and longitudinal stiffeners to the plate thickness. The calculations itself are done by calculating the local moment of inertia of the plates found on plate drawings, provided by AKVA Group. The global moment of inertia is found by using the parallel axis theorem and adding the local moment of inertia.

To get the correct centre of gravity and radius of gyration, the weights used to represent the mass have to be placed on the model in a specific configuration. This is accomplished by solving a global minimization problem with constraints. The function to be minimized is the desired radii of gyration minus the current radii of gyration and the constraints is the restrictions imposed by the location of the centre of gravity. The problem is then solved using MATLAB's global optimization toolbox (Appendix B.1). This is done for three different loading conditions. Namely, light ship (LC0), light-ship with ballast (LC1) and full ship loading condition (LC2), as seen in Fig. 9, 10 and 11, respectively. The full-scale displacements are 318 tons, 596 tons and 1,164 tons for LC0, LC1 and LC2, respectively.

The full-scale barge has a thin hull compared to the scaled model. This makes it difficult to get the correct radii of gyration, especially about the longitudinal axis. Therefore, some of the weights are fitted into the sides of the scaled model (Fig. 9). Data for the additional weights and their placement in the model are summarized in Appendix C. In order to prevent water from entering the model, Plexiglas is mounted on the sides and at the bow of the model. In full ship condition, a roof is also fitted, in order to give additional protection.

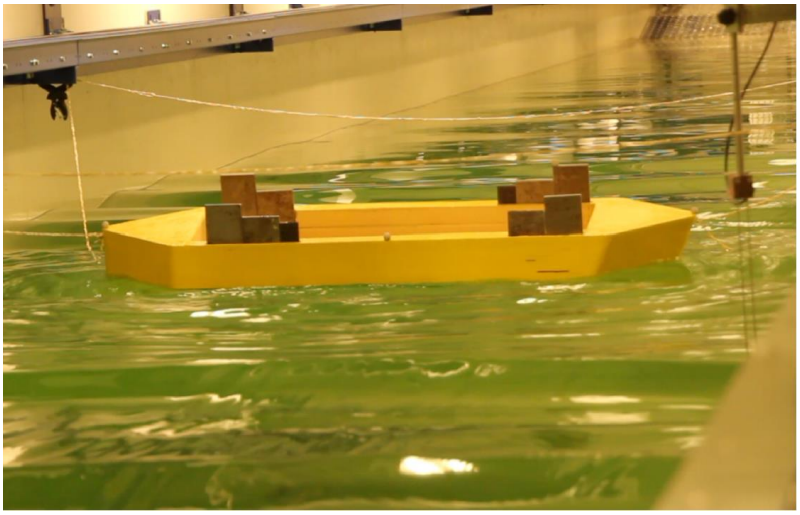

Figure 9: Light ship, loading condition LC0.

Figure 10: Light ship with ballast, loading condition LC1.

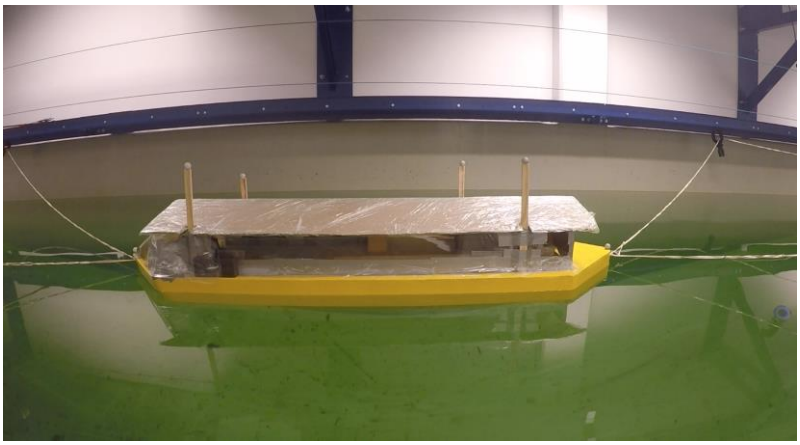

Figure 11: Full ship, loading condition LC2.

Mooring

At operational state, the full-scale barge has moorings made by a combination of chain and rope, moored in muddy seabed or bolts drilled into rocks. The moorings used on the scaled model consists of links of rubber bands, tied together. The rubber bands measure 140 mm x 4 mm. The elastic modulus constant (N/m) of the mooring rubber bands are calculated by Hooke's law,

$$k = -\frac{F}{\Delta L}, \tag{85}$$

where F is the force applied to the elastic rubber band and ΔL is the change in length of the elastic material. The elastic modulus constant of the rubber band is calculated to $33.2\ N/m$. Due to the non-linearity of rubber bands, the elastic modulus is calculated for a specific area, as illustrated in Fig. 12.

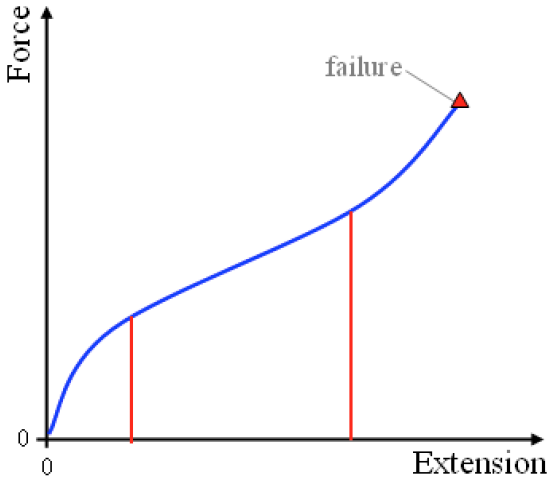

Figure 12: Elastic modulus of rubber bands [33].

During tank testing the mean drift force of the incoming waves pushes the model towards the beach.

The rubber bands stretch until the spring force equals the mean drift forces. The moorings are tied to the bollards and fastened on the top of the glass wall extension at both sides. Tests performed are done in three mooring configurations. The first configuration (DIR1) places the model with starboard side towards the waves (Fig. 13). The second configuration (DIR2) places the model in such a way that the waves hits the model at 30 degrees, measured from the bow toward starboard side (Fig. 14). The third configuration (DIR3) places the model with the bow toward the incoming waves (Fig. 15).

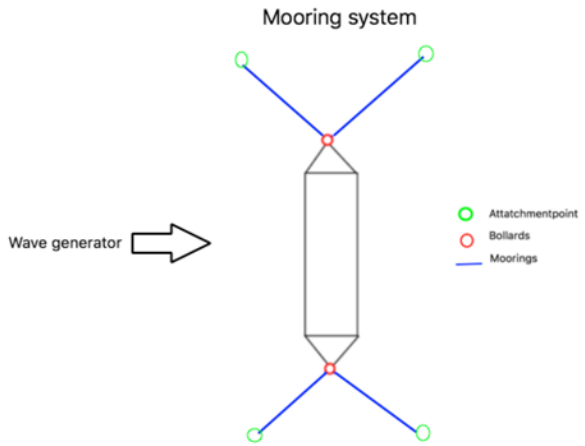

Figure 13: Mooring configuration in DIR1.

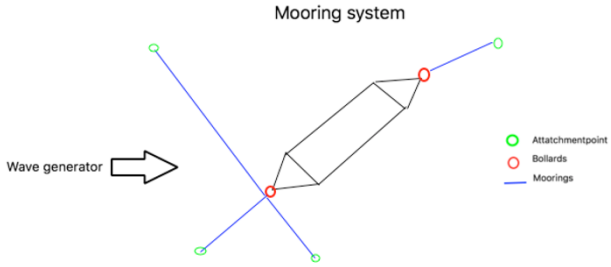

Figure 14: Mooring configuration in DIR2.

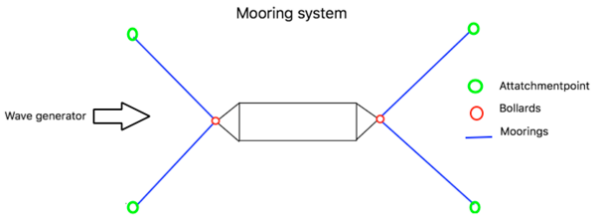

Figure 15: Mooring configuration in DIR3.

9.1.2 Tank Testing

Wave Tank

The tests were carried out in the wave tank at the Department of Mechanical and Marine Engineering, at Western Norway University of Applied Science. The wave tank is designed and delivered by Edinburgh Designs. The tank is 50 meters long, 3 meters wide and 2.2 meters deep. There is a flap based wave generation system in one end (Fig. 16) and a wave-absorbing beach in the other end (Fig. 17). Controlling the wave generation and data collection is done from a control station at the centre of the tank (Fig. 18). The tank has two main applications, measuring motions of a ship in waves and measuring ship resistance by towing the ship with a carriage.

The wave generation system consists of six flaps with a hinge depth of 1200 mm and a width of 500 mm. The paddle system is referred to as a dry back flap system. The motions of the paddles are individual and generates waves in front of the paddles. During wave generation, the reflected waves are measured and the motion of the paddles are changed to absorb the reflections. This provides the wave generation system a repeatability better than 1%. Thus, enabling sequential runs to improve further tests.

Waves reflecting of the tank walls can disturb the desired wave spectrum. To reduce this disturbance, the tank is fitted with a wave-absorbing beach. The beach can absorb up to 90% of the waves and is made of thin metal plates with circular holes. The waves that is not absorbed by the beach will reflect and disrupt the tests. The reflection time varies with different waves.

The paddles are driven by Edinburgh Design's own wave control software. The system consists of two components, Njord Wave Synthesiser and Wave Runtime. Njord Wave Synthesiser is a graphical tool that allows the user to specify the waves to be used in the experiments. In Wave Synthesiser, regular waves, irregular waves, special effect waves, waves with angle, complex composite waves, long and short crested waves can be generated. The waves generated is measured by capacitance gauges and presented as an energy spectrum. By comparing the measured wave spectrum to the desired wave spectrum, the data can be gain corrected in order to generate the desired waves.

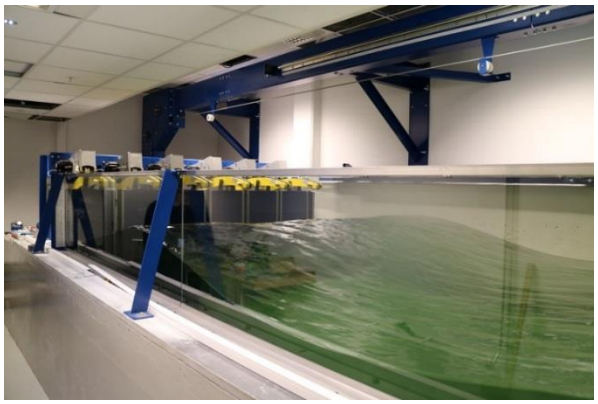

Figure 16: Wave generation paddles.

Figure 17: Wave absorbing beach.

Figure 18: Control station.

Motion Capture System

The lab is fitted with a motion capture system, delivered by Qualisys (Fig 19). The motion capture system measures reflected light, to capture the motions of a model. Small light reflecting bulbs are attached to the model and a body is made in the Qualisys software in order to recognize the motions of the model. After recording motions, the system outputs the data to a text file, which is processed in MATLAB.

Figure 19: Qualisys motion capture system.

Decay Test

To determine the natural frequency of the model, decay tests are performed. Decay tests are done by manually inclining the model, before releasing it and letting the model swing freely in water. By capturing these motions by the Qualisys system and doing a curve fit in MATLAB (Appendix B.5), the natural frequency and damping are obtained. The decay tests are done in LC0.

Regular Wave Test

Regular wave tests are used to obtain the response amplitude operators (RAO) of the model. Determining the RAOs for a floating vessel shows how large motions a vessel will experience in a given sea state. The RAOs are found by sending regular waves with varying frequencies towards the model. By using MATLAB's "Curve Fitting Toolbox", the captured motions and measured wave height are fitted to a Fourier curve. The coefficients from the linear terms (a_1 and b_1) from the fitted Fourier series are used to calculate the response of the wave and the model by,

$$response = \sqrt{a_1^2 + b_1^2}, \tag{86}$$

and the RAO is found by dividing the motion response by the wave response. RAO analysis are performed in LC0, for DIR1 and DIR3.

Irregular Wave Test

In order to know how the model will behave in an actual sea state, the model is tested in irregular seas. The location of the full size barge is known and simulations has been made to determine the 10 and 50 year return period sea states in the area [34]. The 10 and 50 year waves are scaled down for the model tests (Table 1 and 2, respectively). The height and length of the waves are scaled according to Eqn. (83) and the peak period is scaled using,

$$T_{P,M} = \frac{T_{P,F}}{\sqrt{\lambda}}. \tag{87}$$

	Full scale			Model scale		
Direction	Hs [m]	Tp [s]	L [m]	Hs [m]	Tp [s]	L [m]
DIR1	2.4	5	30	0.089	0.962	1.111
DIR2	2.7	5.7	51	0.100	1.097	1.889
DIR3	6.1	14.3	319	0.226	2.752	11.815

Table 1: Wave data for waves with a 10 year return period.

	Full scale			Model scale		
Direction	Hs [m]	Tp [s]	L [m]	Hs [m]	Tp [s]	L [m]
DIR1	2.5	5.1	41	0.093	0.981	1.519
DIR2	2.8	5.8	53	0.104	1.116	1.963
DIR3	7	14.3	319	0.259	2.752	11.815

Table 2: Wave data for waves with a 50 year return period.

The results from the irregular wave tests are used to compute the significant motions, velocities and accelerations. The motions recorded are processed in MATLAB. To remove erroneous data, the raw data is cleaned by a function utilizing the standard deviation of the data (Appendix B.2). In addition, the data is passed through a fourth order Butterworth filter, by inbuilt MATLAB functions. The velocity and acceleration are derived from the motion. The significant response values are found by calculating the response spectrum and extracting the zeroth moment, m_0 (Appendix B.3). From it, the 1/3rd significant value is found by,

$$x_{1/3} = 4\sqrt{m_0} \tag{88}$$

The significant values are compared to equivalent results from MOSES, found in the frequency domain. The MOSES input is available in Appendix D.

Bilge Keel Analysis

One of the interests of AKVA Group was to investigate the effects on roll motion by adding two bilge keels to the model, as illustrated in Fig. 1. However, due to the nonlinearities of viscous damping, these effects are difficult to predict by performing experimental tests on a scaled model. Therefore, this project has investigated these effects by performing simulations in MOSES. The simulations were performed in light ship (LC0), light ship with ballast (LC1) and full ship (LC2) load conditions, in the frequency domain. As the purpose of a bilge keel is to reduce the rolling motion of a ship, the analyses were performed in DIR1 and DIR3. The values of interest are the statistical values. This paper presents and discusses the 1/3rd significant angles, angular velocities and angular accelerations in roll. 1/3rd significant values are the mean of the highest third of the values in question.

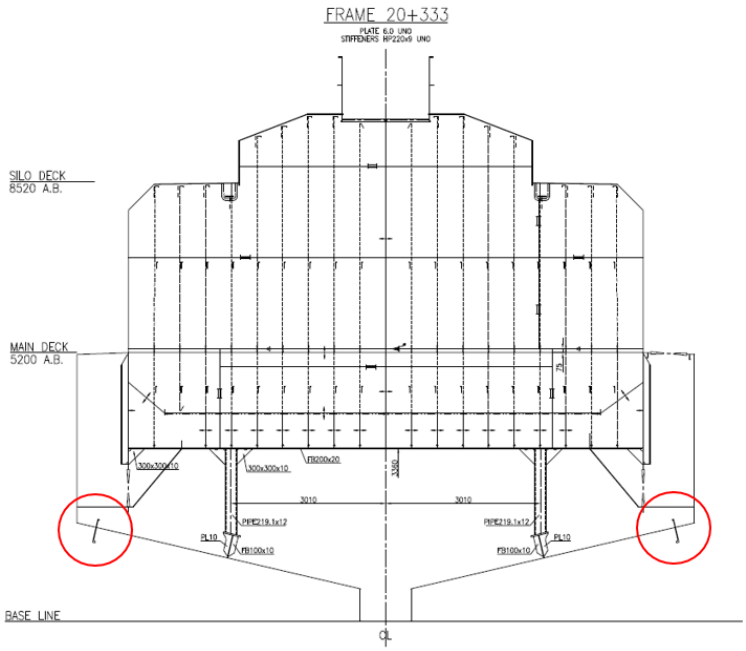

Figure 20: Bilge keels fitted to the barge.

9.2 Experimental Setup: Part II

9.2.1 Gyroscope

There are two identical gyroscopes, the model name is “Super Precision Gyroscope” and they are made by “GYROSCOPE.COM” (Fig. 21). The gyroscopes consist of a disk with a mass of 112g, a gimbal frame and rods and bearings to connect the disk and gimbal. The moment used to spin the disks are provided by two DC motors, powered by 4 1.5V batteries. According to the gyroscope manufacturer the DC motors spins the disks at speeds up to 12,000 RPM.

The precession of the gimbals is provided by two identical continuous servomotors, made by “SPRINGRC”, model number “SM-S3317SR”. Continuous servomotors are used because it can spin further than 180 degrees and are not limited to spin at one speed, as opposed to a regular servo motor.

The servomotors are connected to the gimbals by gears. The ratio of the gears is 56/25 with the larger gear on the gimbal and the smaller pinion on the servo motor. The gyroscopes and servomotors are held in place in two separate cribs (Fig. 22). The disks are spinning continuously and need no control other than being started. The servomotors are controlled using a microcontroller. The microcontroller used is an Arduino UNO and it is controlled by compiling code in Arduino’s own programming language, which is written in C. The code is then loaded on to the Arduino from a computer. The microcontroller can control servos by using Arduino’s Servo library. The speed of the servos can then be adjusted by writing a value between 0 and 180, with 180 being maximum clockwise speed, 0 maximum counter clockwise speed and 90 is a resting

point for the Servo. The angular velocity corresponding to these values has been measured by using a Hall Effect Sensor. The Hall Effect Sensor measures magnetic field and outputs a high signal if it detects a magnetic field. This output can be read by the Arduino.

Figure 21: Super precision gyroscope [35].

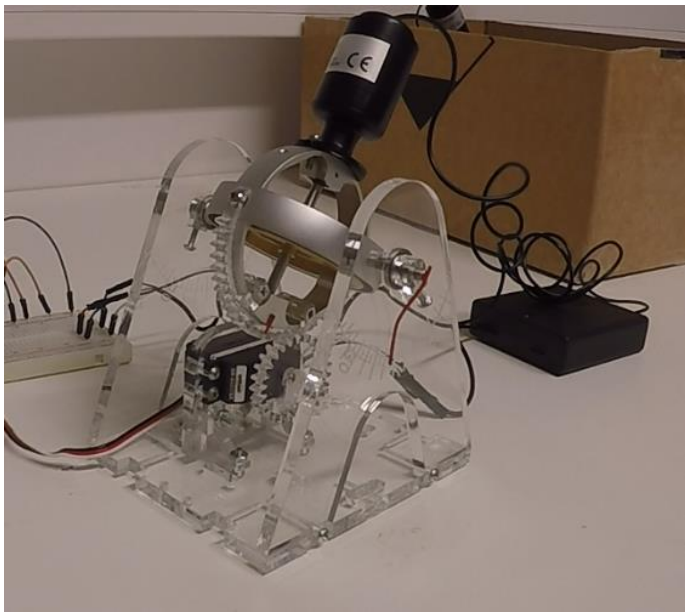

Figure 22: Gyroscope, servomotor, gears and crib.

9.2.2 Experimental Program

Tests are performed using two different programs. The first set of instructions sent to the Arduino rotates the servomotors for 0.8 seconds, at an angular velocity of 6.43 rad/s (Appendix E.1). Accounting for the gear ratio, the rate of precession of the gyroscopes is then 2.87 rad/s. The second program instructs the Arduino to precess the motors at the same angular velocity, but for 0.4

seconds and then wait for 2 seconds before the gyroscopes are precessed in the opposite direction for 0.4 seconds. This process is repeated until the program is stopped (Appendix E). The experimental setup can be seen in Figure 23.

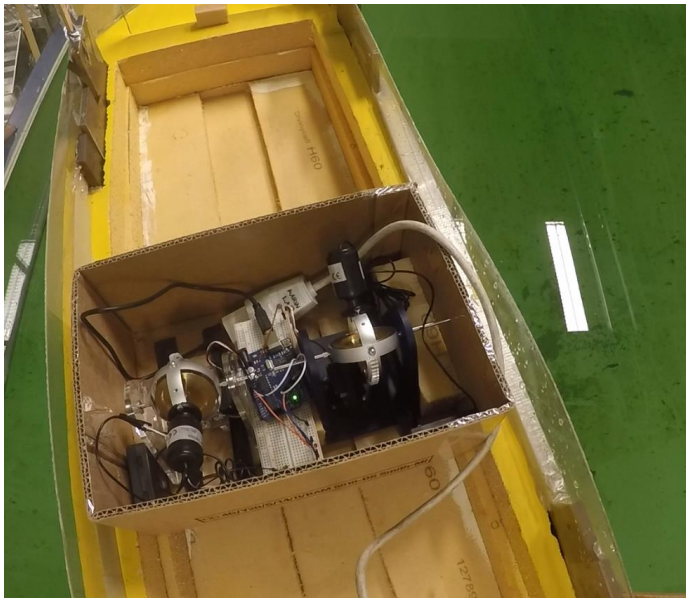

Figure 23: Experimental setup.

10 Results and Discussion

10.1 Theoretical Analysis

Simplified Model

To validate the mathematical model with experiments, the system and equations of motion will be simplified. The reader is first reminded that some simplifications have already been introduced such as the co-location of the two gyro systems at the centre of mass of the boat. This will make it possible to see the effect of several of the system parameters. The equations of motion for the barge installed with two gyroscopic stabilizers will be obtained and solved. Another assumption is made, stating that the two rotors will be identical thin disks moving at opposite prescribed constant angular velocities:

$$J_1^{(3)} = J_2^{(3)} = \frac{J_3^{(3)}}{2}, \qquad J_1^{(5)} = J_2^{(5)} = \frac{J_3^{(5)}}{2}$$

$$J^{(3)} = J^{(5)}, \qquad m^{(3)} = m^{(3)} \tag{89}$$

$$\dot{\psi}^{(3)} = \dot{\psi}^{(5)}, \qquad \psi^{(3)} = \psi^{(5)}$$

$$\delta\dot{\psi}^{(3)} = \delta\dot{\psi}^{(5)} = 0$$

Furthermore, the gimbals will be assumed to be identical, symmetric about all three axes and move with opposite prescribed constant angular velocities,

$$\begin{gathered} J_1^{(2)} = J_2^{(2)} = J_3^{(2)}, \qquad J_1^{(4)} = J_2^{(4)} = J_3^{(4)} \\ J^{(2)} = J^{(4)}, \qquad m^{(2)} = m^{(4)} \\ \dot{\phi}^{(3)} = \dot{\phi}^{(5)}, \qquad \phi^{(3)} = \phi^{(5)} \\ \delta\dot{\phi}^{(3)} = \delta\dot{\phi}^{(5)} = 0 \end{gathered} \tag{90}$$

The barge is also assumed stationary with no translational velocity or acceleration. The focus is on the angular velocity of the barge. Thus,

$$\{\delta q(t)\}^T = \begin{pmatrix} 0 & 0 & 0 & \delta\pi_1^{(1)} & \delta\pi_2^{(1)} & \delta\pi_3^{(1)} & 0 & 0 & 0 & 0 \end{pmatrix} \tag{91}$$

Using the above assumptions, the equations of motions can be reduced to a simpler form, where the subscripts provide information about which rows and columns that must be extracted,

$$[M^*_{44-66}]\left\{\ddot{X}^*_{\underset{6}{4}}(t)\right\} + [N^*_{44-610}]\left\{\dot{X}^*_{\underset{10}{4}}(t)\right\} - F^*_{\underset{6}{4}} = \{0\}, \tag{92}$$

where the following have been defined,

$$M^* = [B(t)]^T[M][B(t)], \tag{93}$$

$$N^* = [B(t)]^T\left([M]\left[\dot{B}(t)\right] + [D(t)][M][B(t)]\right), \tag{94}$$

$$F^* = [B(t)]^T\{Q(t)\}. \tag{95}$$

The framework for deriving the equations of motion of a ship with two active gyroscopic stabilizers has been set. The output of the reduced equation of motion will be a $3x1$ column vector containing the equations of motion for each corresponding angular velocity of the body,

$$\begin{gathered} \left(M^*_{44}\dot{\omega}_1^{(1)} + M^*_{45}\dot{\omega}_2^{(1)} + M^*_{46}\dot{\omega}_3^{(1)}\right) \\ +\left(N^*_{44}\dot{\omega}_1^{(1)} + N^*_{45}\dot{\omega}_2^{(1)} + N^*_{46}\dot{\omega}_3^{(1)} + N^*_{47}\dot{\phi}^{(2)} + N^*_{48}\dot{\phi}^{(4)} + N^*_{49}\dot{\psi}^{(3)} + N^*_{410}\dot{\phi}^{(5)}\right) \\ -F^*_4 = \{0\} \end{gathered} \tag{96}$$

$$\begin{gathered} \left(M^*_{54}\dot{\omega}_1^{(1)} + M^*_{55}\dot{\omega}_2^{(1)} + M^*_{56}\dot{\omega}_3^{(1)}\right) \\ +\left(N^*_{54}\dot{\omega}_1^{(1)} + N^*_{55}\dot{\omega}_2^{(1)} + N^*_{56}\dot{\omega}_3^{(1)} + N^*_{57}\dot{\phi}^{(2)} + N^*_{58}\dot{\phi}^{(4)} + N^*_{59}\dot{\psi}^{(3)} + N^*_{510}\dot{\phi}^{(5)}\right) \\ -F^*_5 = \{0\} \end{gathered} \tag{97}$$

$$\left(M_{54}^{*}\dot{\omega}_1^{(1)} + M_{55}^{*}\dot{\omega}_2^{(1)} + M_{56}^{*}\dot{\omega}_3^{(1)}\right)$$
$$+\left(N_{54}^{*}\dot{\omega}_1^{(1)} + N_{55}^{*}\dot{\omega}_2^{(1)} + N_{56}^{*}\dot{\omega}_3^{(1)} + N_{57}^{*}\dot{\phi}^{(2)} + N_{58}^{*}\dot{\phi}^{(4)} + N_{59}^{*}\dot{\psi}^{(3)} + N_{510}^{*}\dot{\phi}^{(5)}\right) \quad (98)$$
$$-F_5^{*} = \{0\}$$

$$\left(M_{64}^{*}\dot{\omega}_1^{(1)} + M_{65}^{*}\dot{\omega}_2^{(1)} + M_{66}^{*}\dot{\omega}_3^{(1)}\right)$$
$$+\left(N_{64}^{*}\dot{\omega}_1^{(1)} + N_{65}^{*}\dot{\omega}_2^{(1)} + N_{66}^{*}\dot{\omega}_3^{(1)} + N_{67}^{*}\dot{\phi}^{(2)} + N_{68}^{*}\dot{\phi}^{(4)} + N_{69}^{*}\dot{\psi}^{(3)} + N_{610}^{*}\dot{\phi}^{(5)}\right) \quad (99)$$
$$-F_6^{*} = \{0\}$$

With the use of symbolic computational software, most commonly available in MATLAB, the equations can be obtained in terms of the system parameters,

$$\frac{d\omega_1^{(1)}}{dt}\left(J_1^{(1)} + 2J_2^{(4)} + J_3^{(5)}\left(1 + \sin^2\left(\phi^{(4)}\right)\right)\right) + \omega_2^{(1)}\omega_3^{(1)}\left(J_3^{(1)} - J_2^{(1)} + J_3^{(5)}\cos^2\left(\phi^{(4)}\right)\dot{\phi}^{(4)}\right) \quad (100)$$
$$+J_3^{(5)}\dot{\phi}^{(4)}\left(\sin\left(2\phi^{(4)}\right)\omega_1^{(1)} + 2\cos\left(\phi^{(4)}\right)\dot{\psi}^{(5)}\right) - M_1^{(w)} = 0,$$

$$\frac{d\omega_2^{(1)}}{dt}\left(J_2^{(1)} + 2J_2^{(4)} + J_3^{(5)}\right) + \omega_1^{(1)}\omega_3^{(1)}\left(J_1^{(1)} - J_3^{(1)} - J_3^{(5)} + 2J_3^{(5)}\sin^2\left(\phi^{(4)}\right)\right) \quad (101)$$
$$+2J_3^{(5)}\sin^2\left(\phi^{(4)}\right)\dot{\psi}^{(5)}\omega_3^{(1)} - M_1^{(w)} = 0,$$

$$\frac{d\omega_3^{(1)}}{dt}\left(J_3^{(1)} + 2J_2^{(4)} + J_3^{(5)}\left(2 - \sin^2\left(\phi^{(4)}\right)\right)\right)$$
$$+\omega_1^{(1)}\omega_2^{(1)}\left(J_2^{(1)} - J_1^{(1)} - J_3^{(5)} + J_3^{(5)}\cos^2\left(\phi^{(4)}\right)\right) \quad (102)$$
$$-J_3^{(5)}\sin\left(\phi^{(4)}\right)\left(\dot{\psi}^{(5)}\omega_2^{(1)} - \cos\left(\phi^{(4)}\right)\dot{\phi}^{(4)}\,\omega_3^{(1)}\right) - M_3^{(w)} = 0.$$

The equations of motion are nonlinear first order differential equations dependent on the mass properties of the gyroscopes and the body to be stabilized (A, B and C), the two rotors' constant angular velocities $\left(\dot{\psi}^{(3)}, \dot{\psi}^{(5)}\right)$, the two gimbal's constant angular velocities $\left(\dot{\phi}^{(3)}, \dot{\phi}^{(5)}\right)$, and the moments made by the waves $\left(M_1^{(w)}, M_2^{(w)}, M_3^{(w)}\right)$. The controllable parameters or inputs of the system are thus the angular velocity of the rotor and the excitation of the gimbal. The focus is now on the effect of the above parameters and their effect on the amplitude of oscillation on the body.

Reconstruction of Rotation Matrix

The equations of motion for the angular velocity of the ship are dependent on the rotation matrix, $R^{(1)}(t)$, thus the rotation matrix must be known at every time step. The descriptive equation for the rotation matrix $R^{(1)}(t)$ at each time step after integrating the equations of motion is given by,

$$\dot{R}^{(1)}(t) = R^{(1)}(t)\,\overleftrightarrow{\omega^{(1)}(t)}. \quad (103)$$

Eqn. (103) can be integrated analytically from t to $t + \Delta t$ if the angular velocity is constant.

However, that is not the case with the problem at hand. To accommodate for changing angular velocities, the reconstruction can be performed at every time step of the Runge-Kutta integration, assuming the angular velocity stays constant from t to $t + \Delta t$. The mid-point integration method is adopted, using the mean value of the angular velocity. The reconstruction formula, by integrating Eq. (103) is obtained,

$$R(t + \Delta t) = R(t) \exp\left\{\Delta t \overleftrightarrow{\omega(t + \Delta t/2)}\right\}, \tag{104}$$

where the matrix exponential can be calculated using the following expression derived, as derived by Murakami [4],

$$\exp\{t\omega_0\} = I_3 + \left(\frac{\omega_0}{\|\omega_0\|}\right)^2 (1 - \cos(t\|\omega_0\|)). \tag{105}$$

Numerical Solution

Eqns. (100-102) is solved numerically to see the effect of the several controllable parameters of the experimental system. The moment of inertias of the gimbals and rotors used in the experiments have been found in a previous bachelor project [36] to be,

$$J_2^{(4)} \approx 100.32kg \cdot mm^2,\ J_3^{(5)} \approx 74.44kg \cdot mm^2, \tag{106}$$

For the gimbals and rotors, respectively. The mass moment of inertia of the outer body, including the servos, bearings, and microcontroller were found to be,

$$J_1^{(1)} \approx 0.5564kg \cdot mm^2,\ J_2^{(1)} \approx 2.9217kg \cdot mm^2,\ J_3^{(1)} \approx 3.3592kg \cdot mm^2. \tag{107}$$

First, a sinusoidal method of excitation for the gimbal will be prescribed. The gimbal's angular displacement will thus be described by,

$$\phi(t) \approx A_g \sin\left(\frac{2\pi}{T_g}\right) \tag{108}$$

A subscript g is used to signify the terms corresponding to the gimbal. A_g above represents the amplitude of oscillation of the gimbal in radians and T_g is the period. For the first numerical test, A_g is set to be 0.3 radians and T_g is set to be 1 second. The angular velocity $\dot{\phi}(t)$ can be obtained from Eq. (108). The angular velocity of the rotor is kept constant at $\dot{\psi} = 1100\,rad/s$. Substituting the mass parameters and the sinusoidal excitation back into Eqns. (100-102), the equations of motion can be numerically solved. With the fourth order Runge-Kutta, the angular velocities $\omega_1^{(1)}, \omega_2^{(1)}$ and $\omega_3^{(1)}$ be obtained, as shown in Fig. 24.

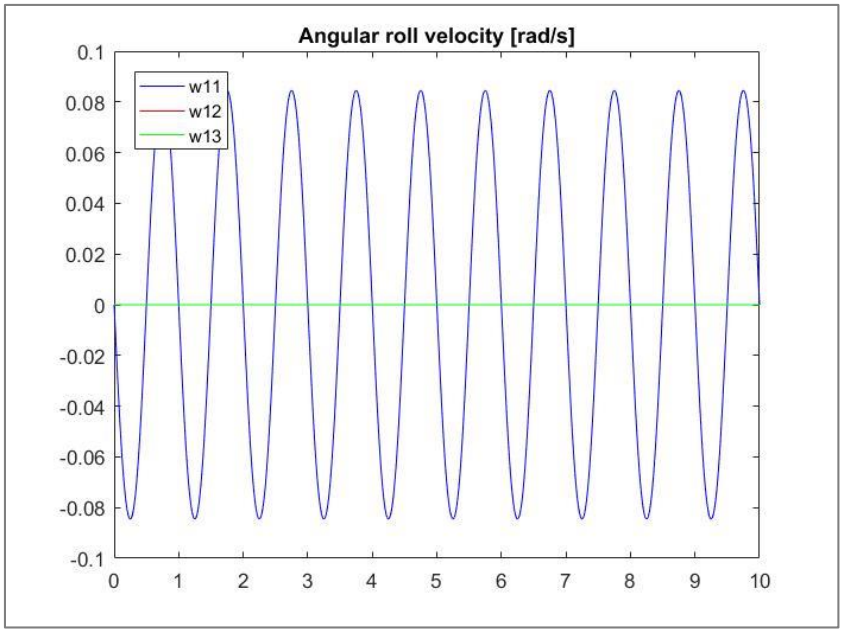

Figure 24: Plot of the angular velocities obtained from the numerical solution.

As shown in Fig. 1, the system consists of a double gyroscope configuration, which cancels the reactionary moments on the deck/platform that would appear if only a single gyroscope were installed. With the dual gyroscope system, the reactionary moments can be cancelled if one of the gyros has the rotor and gimbal excitation operating in reverse. This is shown in Fig. 24, where the angular velocity, $\omega_3^{(1)}$, that causes the yaw of a boat, is equal to 0.

To obtain the angular displacement of the barge as seen in Fig. 25, a method of reconstructing the rotation matrix has been used. Fig. 25 presents the angular displacement for the parameters mentioned above.

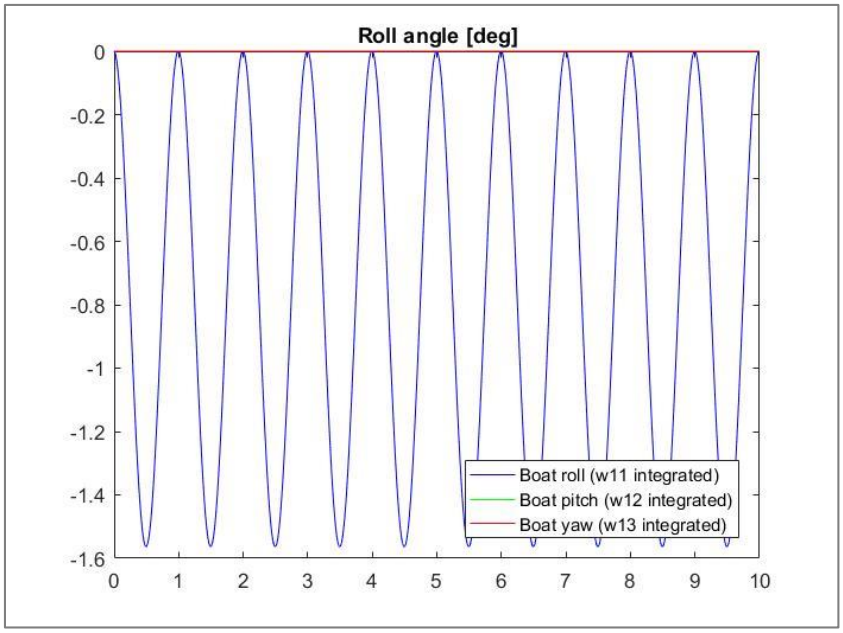

Figure 25: Plot of the angular displacements obtained from the numerical solution.

10.2 Experimental analysis: Part I

10.2.1 Decay Test

17 tests were conducted during the decay testing. Five of these tests are listed in Table 3. The full-scale test results are listed in Table 4. Some of the tests failed to give reasonable values and some of the tests were performed in a faulty way by the test crew. Test 5 yielded the lowest value for natural frequency and test 8 yielded the largest. Test 16 gave the assumed best results, by inspecting the MATLAB plot of the decay test (Fig. 26), where the captured motion is fitted to the curve producing the natural frequency and dampening coefficient.

Test no.	Natural period [s]	Natural frequency [Hz]	Coefficient of Dampening	Duration (sec)
5	0.863	1.159	-0.821	40
2	0.848	1.179	-0.597	35
3	0.857	1.167	-0.737	35
16	0.845	1.183	-0.724	40
8	0.837	1.195	-0.766	40

Table 3: Model results of roll decay tests (LC0).

Test no.	Natural period (sec)
5	4.484
2	4.406
3	4.453
16	4.391
8	4.350

Table 4: Table 3 full-scale values.

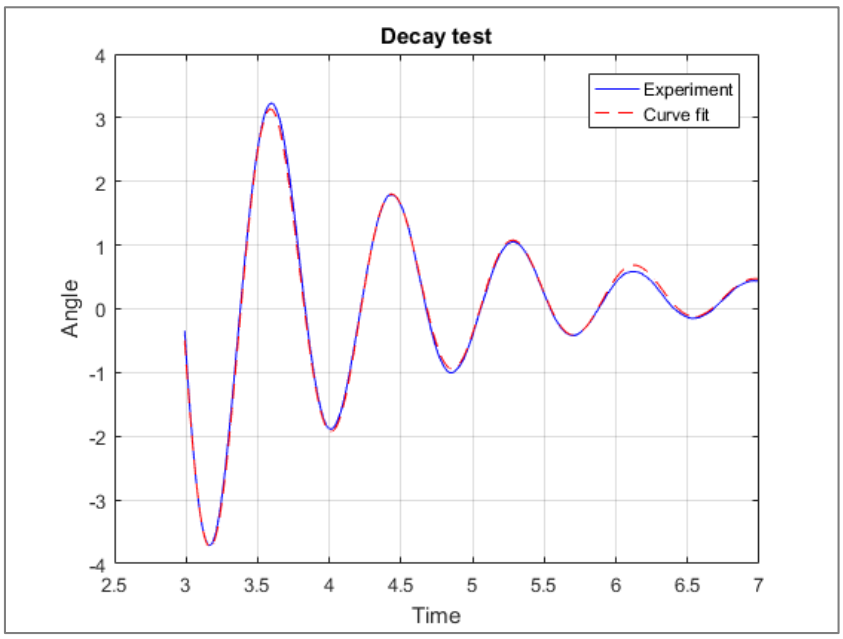

Figure 26: Roll motion and fitted curve to decay test 16 (Table 3).

The standard deviation for the natural frequency is 0.008394137s, when evaluating all 17 tests.

10.2.2 Regular Wave Testing

The results presented in this section are all scaled up to full scale and are performed in LC0. Fig. 27 shows the RAO in pitch for DIR3. The peak period in this test is $4.5s$, with a response of $2.6\,deg/m$. The RAO, in pitch (yellow graph), generated by MOSES is presented in Fig. 28, showing a peak period of $5.6s$ and a response of $4.2\,deg/m$. The values from the testing and the MOSES values are summarized and compared in Table 5.

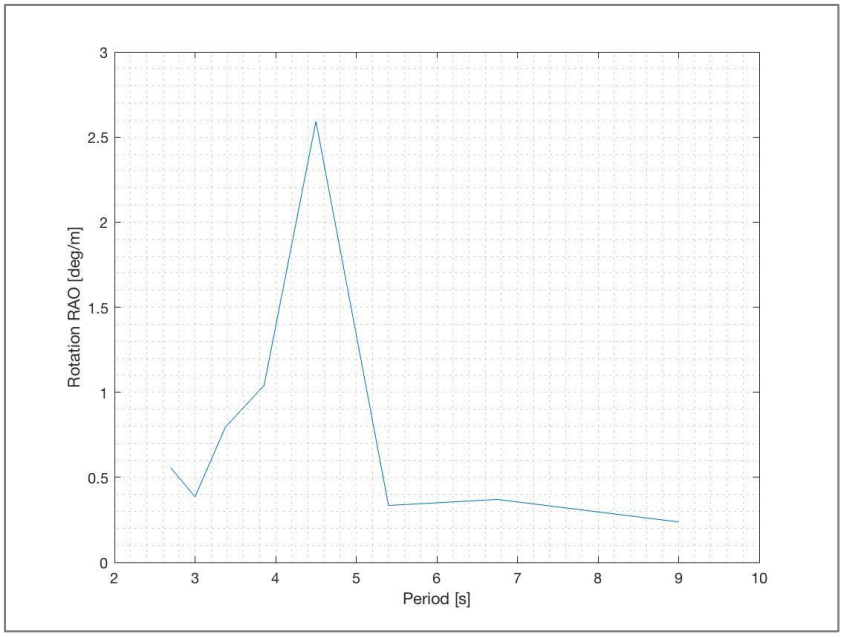

Figure 27: Pitch RAO from test results DIR3, LC0.

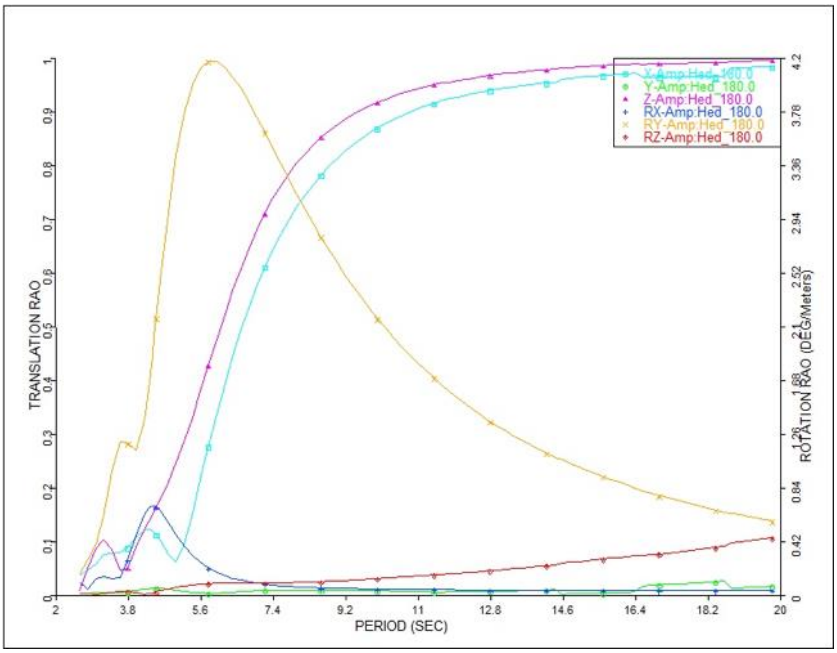

Figure 28: RAO MOSES results DIR3, LC0. Yellow graph is pitch.

	Test	MOSES	Deviation
Peak period [s]	4.5	5.6	24 %
Response [deg/m]	2.6	4.2	62 %

Table 5: RAO test and MOSES results, DIR3, LC0.

The RAO results, in roll, from for DIR1 is presented in Fig. 29 and 30, for the test and MOSES results, respectively. The test results gave a peak period of $5.4s$ and a response value of $14.3\,deg/m$ and the MOSES results gave a peak period of $4.5s$ and a response of $4.2\,deg/m$. These values are summarized and compared in Table 6.

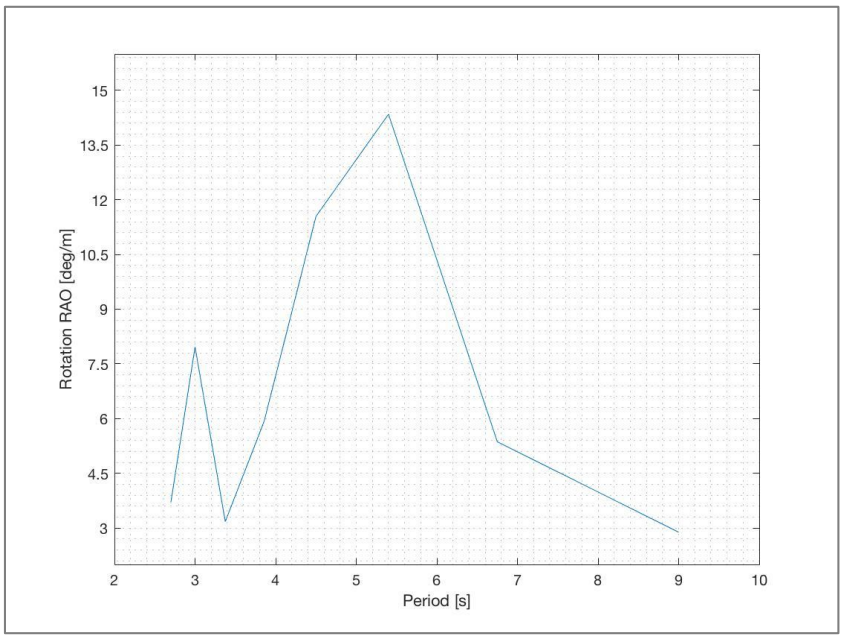

Figure 29: Roll RAO from test results DIR1, LC0.

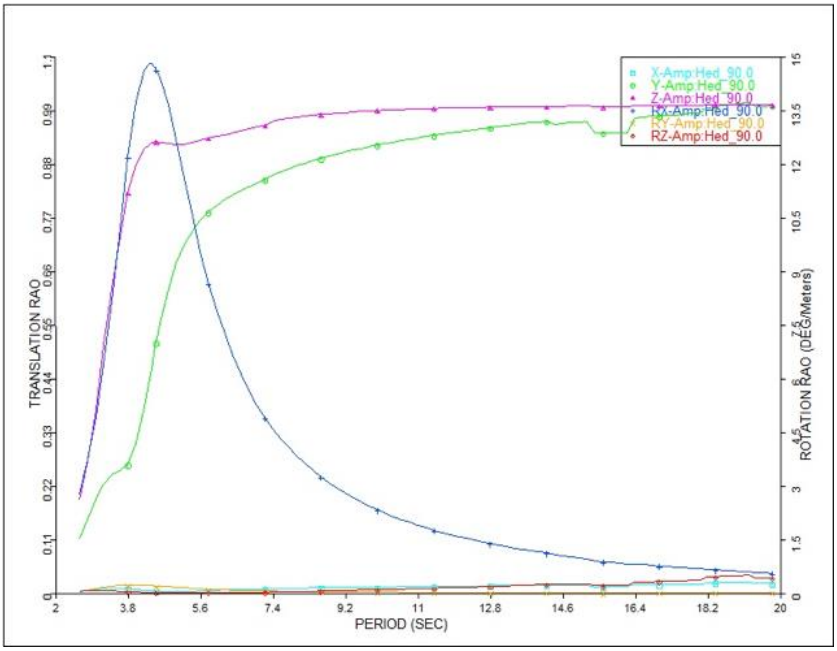

Figure 30: RAO MOSES results DIR1, LC0. Blue graph is roll.

	Test	MOSES	Deviation
Peak period [s]	5.4	4.5	17 %
Response [deg/m]	14.3	4.2	71 %

Table 6: RAO test and MOSES results, DIR1, LC0.

As seen from Table 5 and 6, the peak period of the test results and the simulated data deviates by 24% and 17%, for DIR3 and DIR1, respectively. This could be due to the lack of measurement points around the natural period of the model. The response deviation is 62% and 71% for DIR3 and DIR1, respectively. This large deviation is likely due to non-scalable effects, i.e. viscous forces.

10.2.3 Irregular Wave Testing

Irregular wave tests are performed for DIR1, DIR2, and DIR3, and in all loading conditions. For each direction, there were tested for three different load conditions. For most of the tests, there are done three runs, with a total of 54 test runs. The values presented are the 1/3rd significant response. Results from the tests are presented in Table 7 to Table. 21. The "test result average" is the mean value of the runs performed in the relevant loading condition and direction. The "MOSES result" is the corresponding values, simulated in MOSES. The deviation shows how much the MOSES result deviates from the test results.

Load Condition 0

The results from DIR1 shows that MOSES results have some deviations from the test result for 10 year waves (16%-28%, Table 7). The deviations increase for the 50 year waves (23%-33%, Table

8), which could be due to the increase in non-linear effects with higher waves.

1/3rd significant values	Test result average	MOSES result	Deviation
Roll [deg]	15.39	11.05	28 %
Angular Velocity [deg/s]	19.62	15.04	23 %
Angular Acceleration [deg/s^2]	25.49	21.31	16 %

Table 7: 1/3rd significant response values, DIR1, LC0, r.p. 10.

1/3rd significant values	Test result average	MOSES result	Deviation
Roll [deg]	16.81	11.28	33 %
Angular Velocity [deg/s]	21.35	15.19	29 %
Angular Acceleration [deg/s^2]	27.90	21.35	23 %

Table 8: 1/3rd significant response values, DIR1, LC0, r.p. 50.

For DIR2, the deviations vary from 53% to 100%, for the 10 year waves (Table 9). For the 50 year waves (Table 10), the deviations vary from 21%-44%. This is in contrast to what is found for DIR1 and it could be due to the mooring arrangement for this direction. This direction resulted in relatively large yaw rotations, which will not occur in the MOSES simulation, as it is done in the frequency domain.

1/3rd significant values	Test result average	MOSES result	Deviation
Heave [m]	0.32	0.64	99 %
Velocity [m/s]	0.34	0.68	100 %
Acceleration [m/s^2]	0.40	0.76	88 %
Roll [deg]	2.08	3.66	76 %
Velocity [deg/s]	2.57	4.34	69 %
Acceleration [deg/s^2]	3.49	5.34	53 %
Pitch [deg]	2.64	4.90	85 %
Velocity [deg/s]	2.98	5.64	89 %
Acceleration [deg/s^2]	3.56	6.72	89 %

Table 9: 1/3rd significant response values, DIR2, LC0, r.p. 10.

1/3rd significant values	Test result average	MOSES result	Deviation
Heave [m]	0.50	0.68	37 %
Velocity [m/s]	0.52	0.72	38 %
Acceleration [m/s^2]	0.59	0.79	34 %
Roll [deg]	3.03	3.74	24 %
Velocity [deg/s]	3.55	4.40	24 %
Acceleration [deg/s^2]	4.43	5.38	21 %
Pitch [deg]	3.83	5.08	33 %
Velocity [deg/s]	4.20	5.79	38 %
Acceleration [deg/s^2]	4.73	6.83	44 %

Table 10: 1/3rd significant response values, DIR2, LC0, r.p. 50.

The same tendency is found in DIR3 as in DIR1, with deviations between 3% and 61% for 10 year waves (Table 11) and 48% to 169% for the 50 year waves (Table 12).

1/3rd significant values	Test result average	MOSES result	Deviation
Heave [m]	1.79	2.87	61 %
Velocity [m/s]	1.13	1.45	28 %
Acceleration [m/s^2]	0.79	0.83	6 %
Pitch [deg]	5.32	5.16	3 %
Velocity [deg/s]	4.21	3.81	10 %
Acceleration [deg/s^2]	3.76	3.43	9 %

Table 11: 1/3rd significant response values, DIR3, LC0, r.p. 10.

1/3rd significant values	Test result average	MOSES result	Deviation
Heave [m]	1.22	3.30	169 %
Velocity [m/s]	0.71	1.06	48 %
Acceleration [m/s^2]	0.53	0.96	81 %
Pitch [deg]	3.66	5.92	62 %
Velocity [deg/s]	2.95	4.37	48 %
Acceleration [deg/s^2]	2.66	3.93	48 %

Table 12: 1/3rd significant response values, DIR3, LC0, r.p. 50.

Load Condition 1

In LC1 (Table 13 to 18), the same tendencies are found, as in LC0.

1/3rd significant values	Test result average	MOSES result	Deviation
Roll [deg]	11.52	10.47	9 %
Angular Velocity [deg/s]	14.91	13.53	9 %
Angular Acceleration [deg/s^2]	19.77	17.96	9 %

Table 13: 1/3rd significant response values, DIR1, LC1, r.p. 10.

1/3rd significant values	Test result average	MOSES result	Deviation
Roll [deg]	12.56	10.78	14 %
Angular Velocity [deg/s]	16.07	13.77	14 %
Angular Acceleration [deg/s^2]	21.28	18.09	15 %

Table 14: 1/3rd significant response values, DIR1, LC1, r.p. 50.

1/3rd significant values	Test result average	MOSES result	Deviation
Heave [m]	0.35	0.65	87 %
Velocity [m/s]	0.37	0.69	85 %
Acceleration [m/s^2]	0.43	0.77	79 %
Roll [deg]	1.64	4.58	179 %
Velocity [deg/s]	2.33	5.33	129 %
Acceleration [deg/s^2]	3.48	6.33	82 %
Pitch [deg]	2.95	5.65	92 %
Velocity [deg/s]	3.31	6.47	96 %
Acceleration [deg/s^2]	3.90	7.63	96 %

Table 15: 1/3rd significant response values, DIR2, LC1, r.p. 10.

1/3rd significant values	Test result average	MOSES result	Deviation
Heave [m]	0.53	0.70	32 %
Velocity [m/s]	0.56	0.74	30 %
Acceleration [m/s^2]	0.63	0.80	27 %
Roll [deg]	2.00	4.66	133 %
Velocity [deg/s]	2.75	5.38	96 %
Acceleration [deg/s^2]	3.97	6.34	60 %
Pitch [deg]	3.69	5.85	59 %
Velocity [deg/s]	4.16	6.63	59 %
Acceleration [deg/s^2]	4.89	7.75	59 %

Table 16: 1/3rd significant response values, DIR2, LC1, r.p. 50.

1/3rd significant values	Test result average	MOSES result	Deviation
Heave [m]	1.67	2.88	72 %
Velocity [m/s]	1.10	1.45	32 %
Acceleration [m/s^2]	0.80	0.83	4 %
Pitch [deg]	5.18	5.49	6 %
Velocity [deg/s]	4.26	4.19	2 %
Acceleration [deg/s^2]	3.86	3.86	0 %

Table 17: 1/3rd significant response values, DIR3, LC1, r.p. 10.

1/3rd significant values	Test result average	MOSES result	Deviation
Heave [m]	1.25	3.30	164 %
Velocity [m/s]	0.78	1.66	114 %
Acceleration [m/s^2]	0.55	0.96	74 %
Pitch [deg]	3.68	6.29	71 %
Velocity [deg/s]	2.99	4.80	60 %
Acceleration [deg/s^2]	2.69	4.42	64 %

Table 18: 1/3rd significant response values, DIR3, LC1, r.p. 50.

Load Condition 2

Due to difficulties during the testing in LC2, only two tests were performed. The deviations for DIR1 (3%-15%, Table 19) are similar to the 50 year wave tests in LC0 (Table 8) and LC1 (Table 14). For DIR3, the same tendencies, as for the other loading conditions, are found, with deviations varying between 1% and 70%, and between 44% and 170% for the 10 year wave test and the 50 year wave test, respectively.

1/3rd significant values	Test result average	MOSES result	Deviation
Roll [deg]	2.19	2.50	14 %
Angular Velocity [deg/s]	2.23	2.56	15 %
Angular Acceleration [deg/s^2]	2.87	2.78	3 %

Table 19: 1/3rd significant response values, DIR1, LC2, r.p. 50.

1/3rd significant values	Test result average	MOSES result	Deviation
Heave [m]	1.71	2.89	70 %
Velocity [m/s]	1.13	1.46	30 %
Acceleration [m/s^2]	0.83	0.84	2 %
Pitch [deg]	5.31	5.35	1 %
Velocity [deg/s]	4.46	4.12	8 %
Acceleration [deg/s^2]	4.13	3.86	7 %

Table 20: 1/3rd significant response values, DIR3, LC2, r.p. 10.

1/3rd significant values	Test result average	MOSES result	Deviation
Heave [m]	1.23	3.32	170 %
Velocity [m/s]	0.81	1.68	108 %
Acceleration [m/s^2]	0.67	0.97	44 %
Pitch [deg]	3.67	6.13	67 %
Velocity [deg/s]	3.09	4.72	53 %
Acceleration [deg/s^2]	2.92	4.41	51 %

Table 21: 1/3rd significant response values, DIR3, LC2, r.p. 50.

The 50 year waves have a higher deviation than the 10 year waves for DIR1 and DIR3. This could be due to an increase in non-linear effects with higher waves, which are non-scalable. One way to test this assumption is to test the model in wave conditions with smaller wave heights, however, that is not done in this project.

For DIR2, the opposite tendency is found. It is unclear why this is. The most likely explanation is that this is caused by the mooring system, as previously mentioned.

For roll motion, all deviations are lower than 33%. For heave motion the deviations varies from 61% to 169%. The large variation in heave could be due to difference in the estimated centre of gravity of the model and the actual centre of gravity, as heave motion is influenced by roll and pitch if the assumed centre of gravity is misplaced.

In DIR1, roll angle, angular roll velocity and angular roll acceleration are reduced from LC0 to LC1 and LC2. For the 10 year waves, there is a reduction of 25%, 24% and 22% from LC0 to LC1, in angle, velocity and acceleration, respectively (Table 22). The reduction in for the 50 year waves are shown in Table 23 and Table 24.

1/3rd significant values	LC0	LC1	Reduction
Roll [deg]	15.39	11.52	25 %
Angular Velocity [deg/s]	19.62	14.91	24 %
Angular Acceleration [deg/s^2]	25.49	19.77	22 %

Table 22: Reduction of 1/3rd significant values from LC0 to LC1, DIR1, 10 year waves.

1/3rd significant values	LC0	LC1	LC2
Roll [deg]	16.81	12.56	2.19
Angular Velocity [deg/s]	21.35	16.07	2.23
Angular Acceleration [deg/s^2]	27.90	21.28	2.87

Table 23: Summarization of 1/3rd significant results in DIR1, 50 year waves.

Load condition	Reduction from LC0		
	Roll	Velocity	Acceleration
LC1	25 %	25 %	24 %
LC2	87 %	90 %	90 %

Table 24: Reduction of 1/3rd significant values from LC0, DIR1, 50 year waves.

10.2.4 Bilge Keels

Adding bilge keels to the model reduced the angle, angular velocity and angular acceleration in roll for all load conditions and in all seas. Table 25, 26 and 27 shows the reductions in 1/3rd significant angle, angular velocity and angular acceleration, respectively. The largest reductions are in LC0 and the smallest reductions are in LC2. The reductions in LC1 are between LC0 and LC2, thus the reductions appear to decrease with increasing displacement. However, most of the decrease appears to happen between LC0 and LC1.

Heading	Light ship LC0	Light ship with ballast LC1	Full ship LC2
90 degrees	8 %	7 %	6 %
30 degrees	6 %	1 %	4 %

Table 25: 1/3rd significant roll angle reduction.

Heading	Light ship LC0	Light ship with ballast LC1	Full ship LC2
90 degrees	8 %	7 %	4 %
30 degrees	6 %	2 %	4 %

Table 26: 1/3rd significant angular roll velocity reduction.

Heading	Light ship LC0	Light ship with ballast LC1	Full ship LC2
90 degrees	7 %	7 %	3 %
30 degrees	6 %	3 %	3 %

Table 27: 1/3rd significant angular roll acceleration reduction.

The decrease in roll damping is as expected as the bilge keel roll damping increases linearly with angular velocity [28]. To compare the results presented by Himeno [28], the reduction in roll velocity has been plotted against the angular velocity (Fig. 31). The data has then been fitted linearly, using MATLAB. Upon inspecting Figure 31, a plot showing the angular velocity reduction against the angular velocity with a linear fit, the linear model appears to be a good fit to the data. This is supported by the statistical properties presented in Table 28, which shows the Sum of Squared Errors (SSE) and R-square. A SSE closer to zero implies that there is less random error in the model and the R-square value of 0.9538 means that 95.38% of the variance is accounted for by the model. The residuals of the model presented in Fig. 31 is plotted in Fig. 32. The residual plot

indicates that the model is heteroscedastic because the residuals are increasing with increasing angular velocity. In conclusion, the reduction in angular roll velocity appears to increase with increasing angular roll velocity. However, due to the heteroscedasticity, the model might not be a good predictor for unknown data points. In addition, due to the small number of data points this conclusion is uncertain.

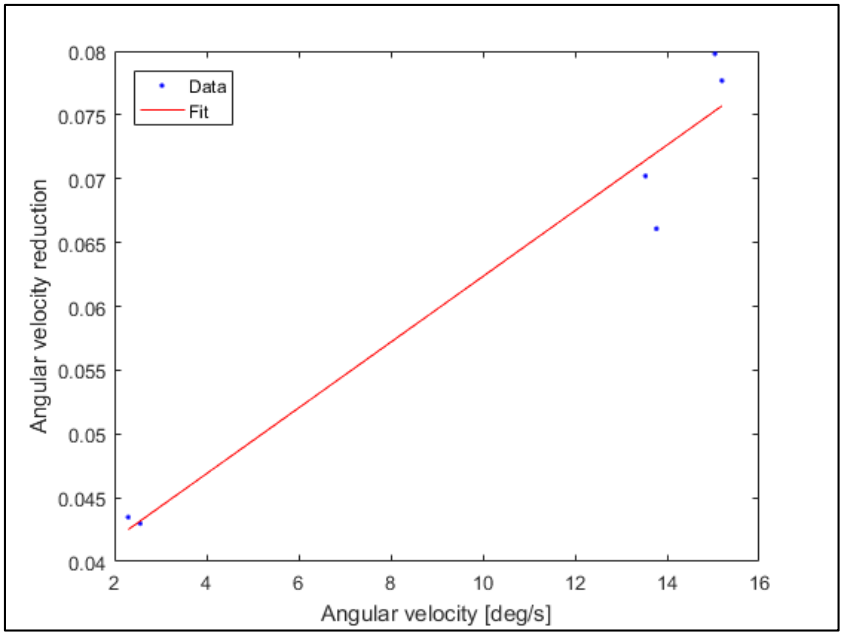

Figure 31: Angular velocity reduction vs. angular velocity.

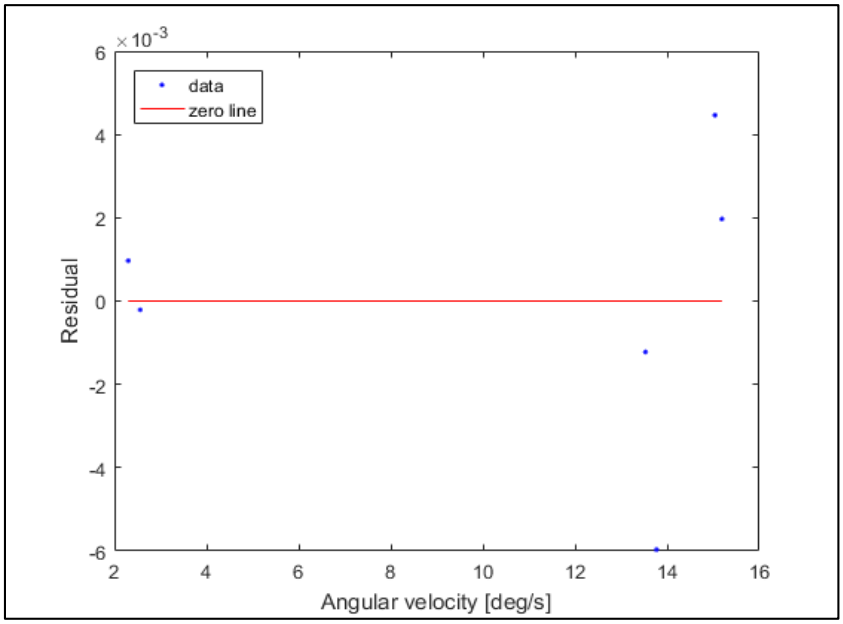

Figure 32: Residual to fitted curve, ref. Fig. 31.

Statistic	Value
SSE	6.19e-05
R-square	0.9538

Table 28: Statistical properties of fitted curve, ref. Fig. 31.

10.3 Experimental Analysis: Part II

A barely perceptible roll of the ship was found, induced by the motion of the gyros. Thus, in this first pass validation of the theory, the authors confirm that there is a qualitative confirmation of roll. However, it is extremely slight, between the prediction of the theoretical model and the actual behaviour. For both of the two tests there are visible results, but the motions are too small to be picked up by the motion capture system. The results did not reflect the numerical analysis, which predicted that the model would experience angular velocities up to 0.08 rad/s and roll angles up to 1.6 degrees. The authors attribute this discrepancy to several factors.

First, the numerical analysis did not take into account the righting moment created by the arm between the buoyancy and gravitational force. This could easily have been done as the theoretical model allows for this. However, such work would have required a more sophisticated processing unit than was found on student laptops. Next, the gyro systems were old and relatively inexpensive. In future tests, a more reliable gyroscopic system is needed with a feedback measurement to ensure that the disks are actually spinning at the high rate claimed by the manufacturer. The motors spinning the gyroscopes are connected to the gyroscopes and their mass is not taken into consideration in the theoretical analysis, where the angular rate of the disks is prescribed. In addition, the gyroscopes are not placed at the centre of mass of the model, as they are in the theoretical analysis. The theoretical model did not account for the role of added mass resisting the motion of the model. The theoretical model did not consider the role of fluid drag on the model or general viscous forces. Again, the MFM allows for the inclusion of such forces, quite readily, as discussed in the companion paper.

11 Conclusion

11.1 Theoretical analysis

The mathematical model of a ship, equipped with dual gyroscopic roll stabilizers has been obtained using the moving frame method. The model has then been simplified to model the experimental setup, in order to further analyse the effects of the system and input parameters. The simplified equations of motion have been solved numerically while varying the inputs. In further work, a direct numerical integration of equation (81) will be conducted. In this phase, the gyros will be properly placed at a generic point on the barge. In addition, added mass, fluid drag and buoyancy should be considered.

11.2 Experimental Analysis: Part I

The decay testing showed that the natural period in roll (LC0) is close to the peak period of the 10 and 50 year waves for DIR1. This produces relatively large motions, velocities and accelerations and some measures should be made in order to alter the natural period. These measures include filling various tanks, in order to raise the radius of gyration. This is confirmed by the irregular wave testing, which shows that roll motions, velocities and accelerations are reduced by between 22% to 25% from LC0 to LC1 and from 87% to 90% from LC0 to LC2. Thus, by ensuring that the various tanks on the barge is not empty, the response of the barge can be reduced. On a feed barge, the amount of feed, ensilage and fuel will vary. However, by using ballasting tanks the operator can alter the response of the barge.

The irregular wave testing and the results obtained from MOSES, shows that the MOSES software can be used as an indication of how the barge will behave.

Analysis performed in MOSES indicates that roll angles are reduced by between 6% and 8%, angular velocities are reduced by between 4% and 8% and angular accelerations are reduced by between 3% and 7%, in DIR1, by installing bilge keels.

11.3 Experimental Analysis: Part II

The moment exerted by the gyroscopes on the model proved too small to obtain any measureable motion of the model. However, observations made by the authors confirmed the qualitative results of the theoretical analysis. The development of the theoretical analysis and the results of the experimental analysis have demonstrated the importance and the limits of simplifications and assumptions in modelling real life systems. These simplifications include neglecting the distance from the gyroscopes to the global centre of mass of the model, neglecting the effects of added mass, drag and viscous forces, righting moment (system stiffness). In addition, the angular rate of the spinning disks has been prescribed in the theoretical analysis.

The microcontroller used were unstable and the servomotors sometimes performs unexpected motions. It is unclear if this is due to the microcontroller or the servo motors itself. Acquiring precise controls and motors would enable the project to include the use of inertial measurement units to measure the motion of the model in real time and minimize these motions by precessing the gyroscopes.

Developing models of real life systems and situations is an important part of an engineer’s work and all such models includes simplifications and assumptions. However, the impact of simplifications is seldom investigated by students. This leaves the students without the ability to assess the significance of each simplification. Further work has the opportunity to examine the impact of the various simplifications. The Moving Frame Method enables students to study real world 3D problems. This, in turn, compels them to study the complexities of systems and to make simplifications and to study the effects of simplifications.

It is suggested that further work on the subject includes design of a model designed for this analysis.

12 References

[1] T. A. Steinset, "Statistisk sentralbyrå," Feb. 2017, https://www.ssb.no/jord-skog-jakt-og-fiskeri/artikler-og-publikasjoner/fra-attatnaering-til-milliardindustri

[2] J. Nyland, H. Teigland, and T. J. Impelluso, "Use of the Moving Frame Method in Dynamics to Model Gyroscopic Control of Small Crafts at Sea. Theory: Part 1 of two papers. IMECE2017-70108," in *ASME 2017 International Mechanical Engineering & Exposition*, Tampa, Florida, 2017.

[3] H. Teigland et al., "Use of the Moving Frame Method in Dynamics to Model Gyroscopic Control of Small Crafts at Sea, Experiment: Part 2 of two papers. IMECE2017-70109," in *Proceedings of the ASME 2017 International Mechanical Engineering & Exposition*, Tampa, Florida, May 2017. http://home.hib.no/prosjekter/dynamics/2017/gyroscope/

[4] H. Murakami, "A Moving Frame Method for Multi-Body Dynamics," *ASME International Mechanical Engineering Congress and Exposition*, No. 4A, 2013.

[5] O. Rios and A. Amini, "Model of a gyroscopic roll stabilizer with preliminary experiments," in *Proceedings of the ASME 2016 International Mechanical Engineering Congress & Exposition*, 2016.

[6] O. Rios and H. Murakami, "A mathematical model of an active gyroscopic roll stabilizer using the moving frame method," in *Proceedings of the ASME 2016 International Mechanical Engineering Congress & Exposition*, 2015.

[7] H. Murakami and O. Rios, "A mathematical model for a gyroscopic ocean wave energy converter, IMECE2013-62834," in *Proceedings of the ASME 2013 International Mechanical Engineering Congress & Exposition*, 2013.

[8] H. Murakami and O. Rios, "A mathematical model with preliminary experiments of a gyroscopic ocean wave energy converter, IMECE2015-51163," in *Proceedings of the ASME 2015 International Mechanical Engineering Congress & Exposition*, 2015.

[9] O. Rios, A. Amini, and D. Ayala, "Development of a gyroscopically driven underwater robot, IMECE2016-67853," in *Proceedings of the ASME 2016 International Mechanical Engineering Congress & Exposition*, 2016.

[10] T. Frankel, *The Geometry of Physics, an Introduction*, 3rd edition, New York, Cambridge, 2012.

[11] J. Denavit and R. Hartenberg, "A kinematic notation for lower-pair mechanisms based on

matrices," *ASME Journal of Applied Mechanics*, pp. 215-221, 1955.

[12] R. P. Paul, "Robot Manipulators: Mathematics, Programming and Control," *The MIT Press, Cambridge*, 1981.

[13] H. Asada and J.-J. E. Slotine, *Robot Analysis and Control*, New York, US, John Wiley and Sons, 1986.

[14] E. J. Haug, *Computer-Aided Kinematics and Dynamics of Mechanical Systems, Vol I: Basic Methods*, Boston, US, Allyn and Bacon, 1989.

[15] P. E. Nikravesh, *Computer-Aided Analysis of Mechanical Systems*, New Jersey, Prentice Hall, 1988.

[16] A. A. Shabana, *Dynamics of Multibody Systems*, 3rd edition, Cambridge, Cambridge University Press, 2005.

[17] E. Cartan, *On Manifolds with an Affine Connection and the Theory of General Relativity*, Napoli, Italy, Bibliopolis, 1986.

[18] V. I. Arnold, *Mathematical Methods of Classical Mechanics*, 2nd edition, New York, Springer-Verlag, 1989.

[19] J. E. Marsden and M. West, "Discrete mechanics and variational integrators," *Acta Numerica*, No. 10, pp. 357-514, 2001.

[20] D. D. Holm, *Geometric Mechanics, Part II: Rotating, Translating and Rolling*, New Jersey, World Scientific, 2008.

[21] T. Lee, N. McClamroch, and M. Leok, "Optimal control of a rigid body using geometrically exact computations on SE(3)," *Proc. IEEE Conf. on Decision and Control*, 2006.

[22] R. W. Brocket, "Robotic manipulators and the product of exponentials formula," *Proc. Int. Symp. Mathematical Theory of Networks and Systems*, 1983.

[23] F. C. Park and R. W. Brockett, "Kinematic dexterity of robotic mechanisms," *Int. J. Robot Res.*, No. 13, pp. 1-15, 1994.

[24] R. M. Murray, Z. Li, and S. S. Sastry, *A Mathematical Introduction to Robotic Manipulation*, Boca Raton, FL, CRC Press, 1994.

[25] B. J. H. van Laarhoven, "Stability Analysis of Parametric Roll Resonance," Eindhoven Univeristy of Technology, Department of Mechanical Engineering, Eindhoven, Traineeship

report 2009.

[26] S. Krüger and F. Kluwe, "A simplified method for the estimation of the natural roll frequency of ships in heavy weather," *HANSA International Maritime Journal*, No. 9, pp. 161-168, 2008.

[27] G. O. G. Avalos, J. B. V. Wanderley, A. C. Fernandes, and A. C. Oliveira, "Roll damping decay of a FPSO with bilge keel," *Ocean Engineering*, No. 87, pp. 111-120, September 2014.

[28] Y. Himeno, "Prediction of Ship Roll Damping - State of The Art," The University of Michigan College of Engineering, 1981.

[29] M. J. v. Kampen, "Bilge Keel Roll Damping," Delft University of Technology, 2015.

[30] W. Froude, "On the rolling of ships," *Transactions of the Institution of Naval Architects*, No. 2, pp. 180-227, 1861.

[31] H. Frahm, "Neuartige Schlingertanks zur Abdämpfung von Schiffrollbewegungen und ihre erforlgreiche Anwendung in der Praxis," *Jahrbuch der Schiffbautechnischen Gesellschaft*, No. 12, p. 283, 1911.

[32] E. P. Bangun, C. M. Wang, and T. Utsunomiya, "Hydrodynamic forces on a rolling barge with bilge keels," *Applied Ocean Research*, Vol. 32, No. 2, pp. 219-232, April 2010.

[33] J. Doshi, "Structural Madness," Ferbuary 2014, http://www.thestructuralmadness.com/2014/02/ductility-and-elasticity.html

[34] T. Lothe, "Numerical Modeling and Evaluation of Extreme Wave Conditions at Brennevinsgrunnen, Rogaland," POLYTEC, 2011.

[35] Gyroscope.com, "Gyroscope.com," 2017, http://www.gyroscopes.co.uk/d.asp?product=SUPER2

[36] M. S. Olsen, A. Nøst, and J. Apeland, "Scale Model of a Gyroscopic Stabilizer," Bergen University COllege, Bergen, Bachelor Thesis 2015.

[37] Yoji Himeno, "Prediction of Ship Roll Damping - State of The Art," The University of Michigan College of Engineering, 1981.

13 Appendix

A. Scale model CAD drawings.
B. MATLAB codes.
C. Scale model weight placement.
D. MOSES input.
E. Arduino codes.
F. 3D web page.